TU Delft

Delft University of Technology

Document Version
Final published version

Licence
Dutch Copyright Act (Article 25fa)

Citation (APA)
Chen, J., Niemeijer, A. R., & Jansen, J. D. (2026). Do Normal Stress Vibrations Stabilize or Destabilize Faults? Experimental Perspectives. *Journal of Geophysical Research: Solid Earth*, *131*(5), Article e2025JB032273. https://doi.org/10.1029/2025JB032273

Important note
To cite this publication, please use the final published version (if applicable).
Please check the document version above.

Copyright
In case the licence states “Dutch Copyright Act (Article 25fa)”, this publication was made available Green Open Access via the TU Delft Institutional Repository pursuant to Dutch Copyright Act (Article 25fa, the Taverne amendment). This provision does not affect copyright ownership.
Unless copyright is transferred by contract or statute, it remains with the copyright holder.

Sharing and reuse
Other than for strictly personal use, it is not permitted to download, forward or distribute the text or part of it, without the consent of the author(s) and/or copyright holder(s), unless the work is under an open content license such as Creative Commons.

Takedown policy
Please contact us and provide details if you believe this document breaches copyrights.
We will remove access to the work immediately and investigate your claim.

This work is downloaded from Delft University of Technology.

Check for updates

JGR Solid Earth

RESEARCH ARTICLE
10.1029/2025JB032273

Do Normal Stress Vibrations Stabilize or Destabilize Faults? Experimental Perspectives

Jianye Chen[1,2,3], **Andre R. Niemeijer**[3], **and Jan-Dirk Jansen**[2]

[1]State Key Laboratory of Earthquake Dynamics and Forecasting, Institute of Geology, China Earthquake Administration, Beijing, China, [2]Faculty of Civil Engineering and Geosciences, Delft University of Technology, Delft, The Netherlands, [3]HPT Laboratory, Department of Earth Sciences, Utrecht University, Utrecht, The Netherlands

Key Points:

- Unstable fault behvaiors can be triggered, synchronized, and reinforced by normal stress perturbations at specific periods
- Rapid and smooth perturbations tend to induce slow, aseismic fault slip
- Cyclic injections, when applied at suitable ranges of period and amplitude, might be a good strategy to mitigate induced seismic risk

Supporting Information:

Supporting Information may be found in the online version of this article.

Correspondence to:

J. Chen,
j.chen3@uu.nl

Citation:

Chen, J., Niemeijer, A. R., & Jansen, J.-D. (2026). Do normal stress vibrations stabilize or destabilize faults? Experimental perspectives. *Journal of Geophysical Research: Solid Earth*, *131*, e2025JB032273. https://doi.org/10.1029/2025JB032273

Received 25 JUN 2025
Accepted 21 APR 2026

Author Contributions:

Conceptualization: Jianye Chen, Andre R. Niemeijer, Jan-Dirk Jansen
Formal analysis: Jianye Chen
Funding acquisition: Jan-Dirk Jansen
Investigation: Jianye Chen
Methodology: Jianye Chen, Andre R. Niemeijer
Project administration: Jan-Dirk Jansen
Resources: Jan-Dirk Jansen
Software: Jianye Chen
Supervision: Andre R. Niemeijer, Jan-Dirk Jansen
Validation: Jianye Chen, Andre R. Niemeijer
Writing – original draft: Jianye Chen
Writing – review & editing: Jianye Chen, Andre R. Niemeijer, Jan-Dirk Jansen

© 2026. American Geophysical Union. All Rights Reserved.

Abstract The effects of stress perturbations on friction are crucial for understanding earthquake triggering. Previous experimental studies have primarily been conducted at room temperature, where fault gouge materials typically exhibit velocity-strengthening and frictionally stable behaviour. In this study, we investigate how variations in effective normal stress (σ_n^e) influence fault (in-)stability by performing σ_n^e-perturbation experiments on simulated carbonate fault gouges under fluid-drained, hydrothermal conditions. Our results indicate that in the velocity-neutral or -weakening regime, perturbing σ_n^e can reinforce frictional instability, leading to accelerated slow slips or enhanced stick-slip events. This effect is particularly pronounced when the excitation period (t_{imp}) approaches or exceeds the characteristic recurrence period (t_r^{pre}) associated with pre-perturbation instabilities. Stress drops of the resulting events can have larger amplitudes than expected from quasi-steady-state. When cyclic perturbations are imposed, slip events tend to synchronize at specific phases when t_{imp} is close to t_r^{pre} — notably between 0.5π and 1π in radian, corresponding to maximum destressing rate and minimum σ_n^e, respectively. Additionally, short-period ($t_{\mathrm{imp}} \ll t_r^{\mathrm{pre}}$) perturbations can induce significant shear stress reduction (or fault weakening), with magnitudes comparable to the stress drops from stick slips, yet they are surprisingly associated with acoustically quiet slow slip, suggesting a stabilizing effect. These findings underscore the critical role of perturbation period in controlling fault response. In the context of induced seismicity, our results imply that cyclic or monotonic fluid injections should be carefully designed, considering both perturbation amplitude and period. Properly turned cyclic injections could potentially mitigate seismic risk by promoting quiet, slow slip over seismic fault slip.

Plain Language Summary Earthquakes happen when stress overcomes friction on a fault. Small stress changes, such as those caused by underground natural gas production or fluid injection, can affect when and how faults slip. Most past experiments were done at room temperature, where faults tend to slip slowly and stably. In this study, we tested how changes in effective normal stress (the force pressing the fault surfaces together) affect fault slip under hot, fluid-filled conditions, similar to those in the deep subsurface. We found that when the fault is already unstable, stress changes can make slip happen faster or trigger sudden slip events. These effects depend on how frequently the stress changes occur—if the timing is right, they can make slip more violent. Short, rapid stress changes can also weaken the fault without much seismicity, while sudden stress jumps can trigger seismic events. Our findings suggest that controlling the timing and magnitude of normal stress changes, such as via fluid injection in geothermal or wastewater projects, may help reduce triggered and induced earthquake risk.

1. Introduction

Active tectonic fault zones are continuously subjected to variations in effective normal stress (σ_n^e) that affect their strength and frictional instability. For example, fault slip can induce changes in normal stress (σ_n) and in fluid pressure (p_f) wherever inhomogeneities exist on a fault, for example, due to geometric irregularities in the fault or heterogeneous materials (Ma et al., 2008; Ranjith & Rice, 2001). Earthquakes can alter the static stress surrounding the rupture zone and also send seismic waves that propagate thousands of kilometers to influence the far stress field (Hill et al., 1993; West et al., 2005). External periodic sources such as solid Earth tides can also modify the evolution and pattern of fault zone stresses (Bindschadler et al., 2003; Tanaka et al., 2012). Fluid pressures within a fault zone are expected to vary cyclically during earthquake cycles too, promoting or delaying failure of the fault (Segall & Rice, 1995). Seasonal impoundment and discharge of reservoirs have similar effects (Gao

21699356, 2026, 5, Downloaded from https://agupubs.onlinelibrary.wiley.com/doi/10.1029/2025JB032273 by Tu Delft, Wiley Online Library on [27/05/2026]. See the Terms and Conditions (https://onlinelibrary.wiley.com/terms-and-conditions) on Wiley Online Library for rules of use; OA articles are governed by the applicable Creative Commons License

et al., 2000; Lowry, 2006). Moreover, human activities such as hydrocarbon and geothermal energy production can change the stress fields around and within faults and possibly induce earthquakes (e.g., Ellsworth, 2013).

Much insight into the processes governing earthquake triggering has been gained from previous laboratory experiments and theoretical developments. Early experimental studies addressing how fault strength and stability respond to σ_n^e-perturbations were performed on bare rock surfaces under lab dry conditions (Bureau et al., 2000; Cochard et al., 2003; Linker & Dieterich, 1992; Olsson, 1988; Prakash, 1998). These experiments involved step- and cyclically varying changes in external normal stress (σ_n) imposed on a steadily sliding fault. Linker and Dieterich (1992) showed that the frictional response to a rapid change in σ_n is a multistage process, consisting of (1) an "immediate" response along the elastic-loading path, followed by (2) a "transient" evolution approaching a new steady state. To account for these effects, Linker and Dieterich extended the classical rate-and-state-dependent friction (RSF) laws to describe the evolution of friction in response to σ_n changes (hereafter referred to as the LD formulation). Arguing that a sudden change in σ_n would alter the state variable, an extended state equation was postulated:

$$\frac{d\theta}{dt} = 1 - \frac{v\theta}{D_c} - \alpha \frac{\theta}{b\sigma_n} \frac{d(\sigma_n)}{dt} \text{ (from Dieterich's equation)}, \quad (1)$$

where v is slip velocity; θ is the state variable (units of time), b is the constitutive parameter describing the evolution effect, and D_c is a characteristic sliding distance for state evolution. The last term including the empirical factor α was introduced to describe the evolution of state, and thus friction, following a σ_n-change. Prakash (1998) observed that following a σ_n step change, shear stress did not respond immediately; rather it evolved gradually to a new steady state. An alternative modification of the RSF framework has been proposed accordingly (Prakash, 1998).

Later laboratory studies explored a variety of materials (bare-rock surfaces, simulated fault wear products or gouges) and σ_n^e perturbation patterns (stepping, pulse, and oscillations; varying σ_n or p_f) under lab-dry or wet conditions (Bartlow et al., 2012; Boettcher & Marone, 2004; Chen et al., 2024; Colledge et al., 2023; Dang et al., 2018; Griffa et al., 2013; Hong & Marone, 2005; Huang et al., 2016; Johnson et al., 2012; Kilgore et al., 2012, 2017; Lockner & Beeler, 1999; Shreedharan et al., 2019; Yu et al., 2024). Boettcher and Marone (2004) varied the amplitude of normal stress oscillations, and showed that a larger amplitude produces a pronounced reduction in shear strength, as confirmed in the recent experiments by Dang et al. (2018).

The general conclusion is that time-varying σ_n^e causes a transient response in friction, though triggering or promotion of unstable slip has rarely been observed (Beeler & Lockner, 2003; Boettcher & Marone, 2004; Yu et al., 2024). We propose that this is at least partly because most previous experiments were performed at room temperature, where rock-forming minerals generally fall in the v-strengthening regime. The fault is then frictionally stable (Scholz, 2019), which implies that any perturbation that favors unstable slip would be suppressed even if the fault is under critically stressed conditions close to failure. Progress has been impeded here by the fact that it is technically challenging to investigate σ_n^e-effects under crustal temperature and fluid pressure conditions where frictional fault slip is v-weakening and potentially unstable (Jia et al., 2021; Pignalberi et al., 2024). Although instabilities in natural fault gouges are more commonly associated with elevated temperatures (where velocity-weakening behavior often emerges), it is important to note that certain materials—including glass beads, quartz, gypsum, and halite gouge—do exhibit velocity-weakening friction and associated unstable behavior (e.g., stick-slip) at room temperature under specific loading conditions (Johnson et al., 2008; Leeman et al., 2016; Niemeijer et al., 2010; Shimamoto et al., 1980). A recent experimental study by Chen et al. (2024) investigated the effects of varying effective normal stress on carbonate gouge friction under hydrothermal conditions. Their results show a significant reduction in mean shear strength when applying relatively fast (0.2–5 Hz) oscillations, accompanied by anelastic (time-dependent but recoverable) dilatation. Such dilatation was found to be consistent with a decrease in acoustic transmissivity (Yu et al., 2024). Chen et al. (2024) also pointed out that varying the temperature, and thus the propensity for v-weakening and instability, can help distinguish between existing friction models that seem to fit results obtained at room temperature equally well.

There have been a growing number of experimental studies focusing on the effects of fluid pressure (p_f) on fault stability (Cappa et al., 2019; Chanard et al., 2019; French et al., 2016; Noël, Passelègue, et al., 2019, Noël, Pimienta, & Violay, 2019; Passelègue et al., 2018; Scuderi & Collettini, 2016; Scuderi et al., 2017; Wang,

21699356, 2026, 5, Downloaded from https://agupubs.onlinelibrary.wiley.com/doi/10.1029/2025JB032273 by Tu Delft, Wiley Online Library on [27/05/2026]. See the Terms and Conditions (https://onlinelibrary.wiley.com/terms-and-conditions) on Wiley Online Library for rules of use; OA articles are governed by the applicable Creative Commons License

Kwiatek, Rybacki, Bonnelye, et al., 2020; Xing et al., 2019; Zhuang et al., 2016). The results showed that fault slip behavior is controlled by the stress state acting on the fault and that fluid pressurization can trigger dynamic instability (i.e., significant increase in slip velocity). Recent field observations suggest that cyclic fluid injection might trigger different seismic responses within reservoir formations compared to monotonic fluid injection (Yoon et al., 2014; Zang et al., 2013). Increasing complexity has since been added to the strategy of applying cyclic stimulation (Zang et al., 2018). While these experiments are directly relevant to induced seismicity, it would be useful to explore the effects of small-amplitude perturbations by systematically time-varying the normal stress under dry or fully drained conditions (e.g., Colledge et al., 2023), thus eliminating some of the complexities caused by temporal and spatial fluid pressure variations, for example, due to pressure diffusion and permeability enhancement (Candela et al., 2014).

To provide the crucial frictional data missing from previous experiments primarily conducted at room temperature, in this study we performed gouge-shearing experiments at crustal temperature, normal stress, pressure, and well-drained pore fluid conditions, to determine how σ_n^e-variations affect the frictional stability of a gouge-filled fault. We used calcite gouge, whose frictional behavior is well-constrained from previous studies. We focused on the v-neutral and v-weakening friction regimes. Different modes of perturbation in σ_n^e were applied to the fault under conditions showing different pre-perturbation behaviors (i.e., stable sliding, small-amplitude fluctuations, or stick-slip behavior). By analyzing the responses in shear stress, gouge layer thickness, and acoustic emissions, we found that the excitation period of normal stress perturbations plays an essential role in fault behavior. Perturbations near the system's inherent period (i.e., the period associated with pre-perturbation instabilities) enhance and modulate fault instability, while higher-frequency oscillations promote slow, acoustically silent slip. These findings improve our understanding of normal stress effects and have important implications for fault stability in geo-reservoirs.

2. Material and Method

2.1. Material

In this study. We tested two types of simulated carbonate fault gouges. The first was prepared from calcite single crystals (Iceland spar quality), while the second was derived from a natural carbonate fault breccia collected from an exposure along the Longmenshan Fault, which hosted the 2008 Mw 7.9 Wenchuan earthquake in Sichuan, China. X-ray diffraction analysis revealed that the single-crystal calcite gouge consists of 98% calcite plus ≤2% dolomite. The natural fault sample contains 68% calcite and 29% dolomite, with minor amounts of clay and quartz. To create the simulated fault gouges, both materials were crushed and sieved to produce fine powders. The resulting grain sizes were ≤28 μm for the pure calcite gouge and ≤35 μm for the breccia-derived gouge, consistent with the grain size ranges used in previous studies (Chen et al., 2015; Verberne et al., 2013).

2.2. Experimental Apparatus

We conducted shear experiments on simulated fault gouges using the hydrothermal, rotary shear apparatus at Utrecht University. As shown in Figure 1a, the apparatus consists of a compound pressure vessel, housing a pair of opposing rotary pistons that sandwich a thin layer of simulated fault gouge. The pressure vessel is mounted onto an Instron 1362 electromechanical loading frame, designed for low-rate fatigue testing, which enables relatively high-frequency control of normal load. The vessel is pressurized with water, which serves as pore fluid, with pressure being controlled using a custom-built servo-controlled pump.

Since the upper piston is fluid pressure-compensated, the effective normal stress ($\sigma_n{}^e$) is defined in terms of the externally applied normal load minus the resistance offered by the three dynamic O-ring seals (marked in red in Figure 1a). Due to the high porosity of a carbonate gouge (~18%, Chen & Spiers, 2016) and the short diffusion distance (<1 mm), we assume well-drained fluid conditions and uniform transmission of fluid pressure within the gouge. This means that variations in external normal stress (σ_n) are equivalent to variations in $\sigma_n{}^e$.

To measure displacement normal to the fault (i.e., compaction/dilatation), we used a high-resolution linear variable differential transformer (LVDT), with 0.1 μm resolution, mounted on the lower forcing piston (technically on the side of the base holding the pressure vessel), and an additional LVDT with 1.0 μm resolution located at the bottom of the Instron ram (Figure 1a).

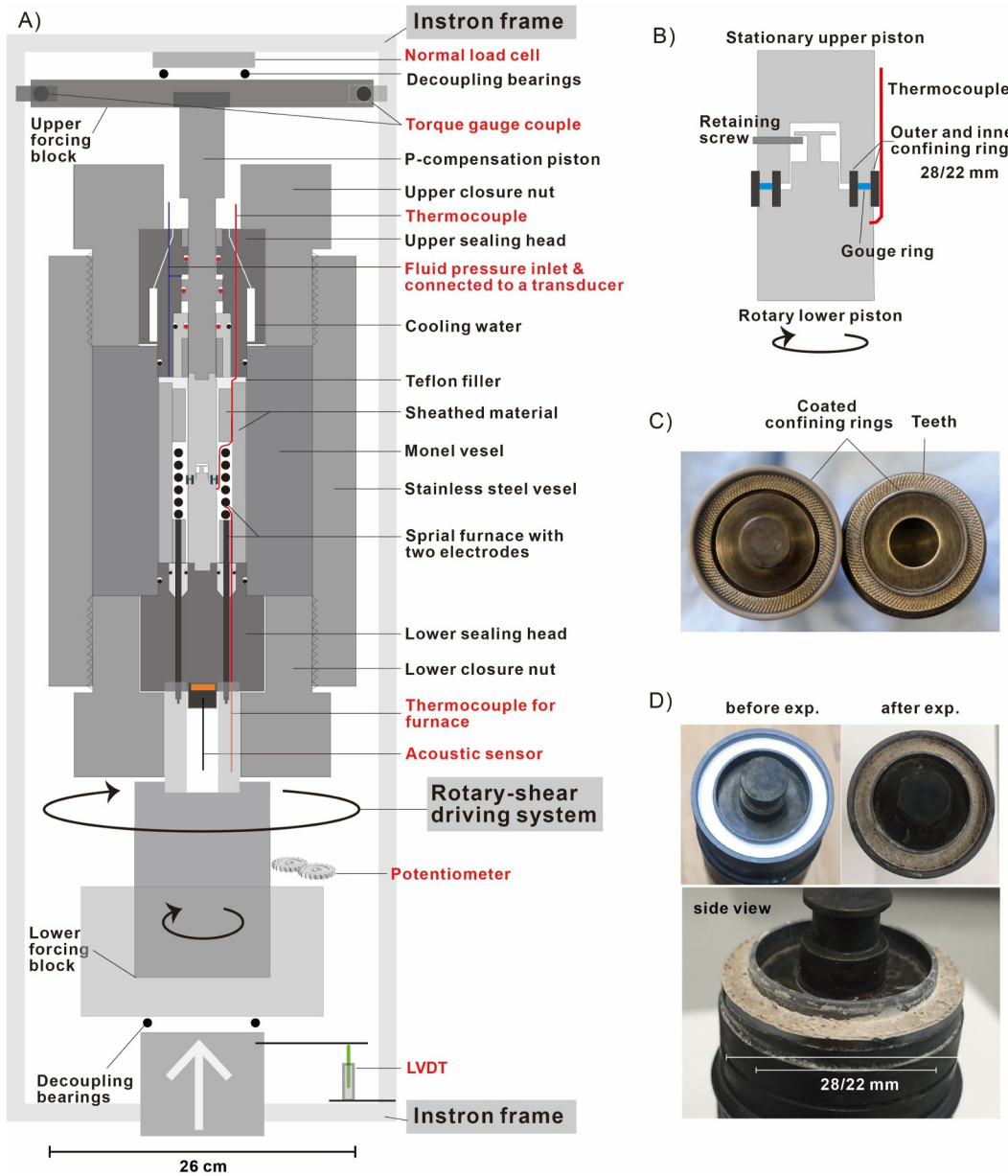

Figure 1. Schematic of the Utrecht ring-shear hydrothermal pressure vessel and sample assembly. Panel (a) cross-section of the pressure vessel mounted on an Instron frame, with red text indicating measured quantities. Panel (b) close-up of the sample-piston assembly. Panel (c) top view of the piston pair and confining rings. Panel (d) top and side views of the gouge layer before and after an experiment (u829).

Shear deformation is imposed by rotating the vessel and the internally fixed lower piston, while the upper, pressure-compensated piston remains stationary. The rotation is driven by an electromotor via a gearbox system (Figure 1a). Ball bearings positioned above and below the driving blocks decouple the vessel's rotation from the Instron frame. Torque and axial normal load were monitored using sensors mounted on the upper forcing block (or torque bar). Shear displacement was measured with a potentiometer attached to the lower driving block. To assess the dynamics of frictional stability, two PZT sensors—with dominant frequencies of 1 MHz and 4 kHz, respectively—were integrated into the setup: one was spring-loaded directly underneath the bottom piston, and the other was spring-loaded ~20 mm to the side (Figure 1a; Zhou, 2020). Silica gel was applied to enhance the acoustic coupling. We verified that the 1 MHz sensor exhibits robust sensitivity across a broad frequency range, including as low as 1 kHz; for clarity and focus, we present only data from this 1 MHz sensor in the study.

21699356, 2026, 5, Downloaded from https://agupubs.onlinelibrary.wiley.com/doi/10.1029/2025JB032273 by Tu Delft, Wiley Online Library on [27/05/2026]. See the Terms and Conditions (https://onlinelibrary.wiley.com/terms-and-conditions) on Wiley Online Library for rules of use; OA articles are governed by the applicable Creative Commons License

Table 1
Experimental Conditions and General Behaviors

Exp.	Material	T (°C)	$\overline{\sigma}_n^e$ (MPa)[a]	p_f (MPa)	v-dep[b]	Initial behavior	t_r^{pre} (s)[c]	Pertu. Modes[d]	AE
u574	Fault breccia	110	50|60|80|100|140|180	15	v-neu.	Stable sliding	–	NSO	–
u829	Iceland spar calcite	80	150	3	v-w	Fluctuating	6–13	NSS, NSP, NSO	√
u828	Iceland spar calcite	100	150|100	15	v-w	Fluctuating	5–10| 5–9	NSS, NSO	√
u589	Fault breccia	150	50	50	v-w	Fluctuating	2–5	NSO	–
u589	Fault breccia	200	50	50	v-w	Fluctuating	10–18	NSO	–
u589	Fault breccia	300	50|100|180	50	v-w	Stick slipping	4–7| 6–14| 20–25	NSO	–

[a]$\overline{\sigma}_n^e$ is the base level of the (effective) normal stress before imposing perturbations. [b]v-dep. is velocity dependence of steady-state friction determined via v-step tests before perturbation (v-w = velocity weakening; v-s = velocity strengthening; v-neu, velocity neutral). [c]Recurrence period of the friction instability before imposing perturbations. Note that the loading velocity was consistently 1 μm/s in all experiments. [d]Perturbation modes of normal stress (Pertu., perturbation; NSS, normal stress step; NSO, normal stress oscillations; NSP, normal stress pulse). AE, acoustic emission measurement.

Compared to conventional friction experiments using saw-cut or direct-shear assemblies located inside a triaxial testing vessel, the present hydrothermal rotary shear apparatus offers key advantages: It enables rapid variations in (effective) normal stress while simultaneously applying high fluid pressure and temperature conditions. It thus allows for testing in potentially unstable v-weakening deformation regimes, which is challenging in other apparatus types. The Instron control platform enables normal load variations in different modes (i.e., stepped, square, "sawtooth" and sinusoidal) and at various frequencies. By tuning the Instron PID settings, we achieved precise normal load control at frequencies above 10 Hz, and stable sinusoidal/sawtooth oscillations up to 5 Hz, owing to a high normal stiffness of the system (up to 360 MPa/mm). Amplitude variations up to 20% of the base level were stable, though larger amplitudes occasionally led to overshooting. In this study, the shortest oscillation period applied was 0.2 s, longer than the response times of all system components of the apparatus, including normal load (Instron), shear drive (servo motor), and fluid pressure (servo pump) controls.

2.3. Experimental Conditions and Procedures

Previous studies have constrained the frictional behavior of carbonate gouges as a function of temperature (T), load-point velocity (v_{imp}), and effective normal stress (σ_n^e) (e.g., Chen et al., 2015; Verberne et al., 2013, 2015). A transition in the rate dependence of steady-state friction occurs at 80°C, from v-strengthening to v-weakening with increasing temperature. Below 80°C, stable sliding is consistently observed. Between 80 and 200°C, the deformation mode varies from stable sliding to sliding with small-amplitude fluctuations, depending on v_{imp}, σ_n^e and apparatus stiffness. For temperatures ranging from 200°C to 550°C, carbonate gouges exhibit stick-slip behavior across a wide range of conditions. Beyond 550°C, ductile deformation starts to dominate, particularly under low loading velocities and high effective normal stress (Chen et al., 2020; Verberne et al., 2017).

In this study, experimental conditions were carefully chosen to achieve different types of frictional behavior before imposing σ_n^e-perturbation. A total of four experiments were performed (Table 1). The experimental conditions were as follows: Temperatures were maintained constant at 80–110°C for most experiments, except for one experiment (u589) where it was increased stepwise from 150°C to 300°C. The base level of effective normal stress ($\overline{\sigma}_n^e$) varied from 50 to 180 MPa. Pore-fluid pressures (p_f) were 15 MPa, except in one experiment (u829) where a p_f of 3 MPa was used to assess seal friction effects on shear strength. Also in u589, a high p_f of 50 MPa was applied to prevent vaporization at high temperatures. All the perturbation tests were performed at a constant loading velocity (v_{imp}) of 1 μm/s.

In each experiment, ~0.65 g of simulated fault gouge powder was distributed between the grooved ring located at the ends of the opposing René-41 Ni-alloy pistons, and confined by an outer (28 mm) and inner (22 mm) confining ring (Figure 1b). The confining rings were lubricated using Molykote D-321R anti-friction coating to minimize wall friction (Figure 1c). After mounting the sample assembly into the vessel and placing the vessel in the Instron frame, initial (effective) normal stress (σ_n^e), pore-fluid pressure (p_f), and temperature (T) were applied. After stabilization, samples were sheared at a constant v_{imp} of 1 or 10 μm/s for ~7.0 mm displacement, followed by a serious of v-steps to evaluate friction rate dependence. The final step of velocity was always set to

21699356, 2026, 5, Downloaded from https://agupubs.onlinelibrary.wiley.com/doi/10.1029/2025JB032273 by Tu Delft, Wiley Online Library on [27/05/2026]. See the Terms and Conditions (https://onlinelibrary.wiley.com/terms-and-conditions) on Wiley Online Library for rules of use; OA articles are governed by the applicable Creative Commons License

21699356, 2026, 5, Downloaded from https://agupubs.onlinelibrary.wiley.com/doi/10.1029/2025JB032273 by Tu Delft, Wiley Online Library on [27/05/2026]. See the Terms and Conditions (https://onlinelibrary.wiley.com/terms-and-conditions) on Wiley Online Library for rules of use; OA articles are governed by the applicable Creative Commons License

be 1 μm/s. Based on the behavior obtained, T and $\sigma_n{}^e$ were adjusted to achieve the desired frictional behavior before imposing $\sigma_n{}^e$-perturbations. Subsequently, different types of normal stress perturbations were applied, including normal stress steps (NSS), pulses (NSP), and oscillations (NSO) with sinusoidal or "sawtooth" waveforms. Facilitated by the theoretically infinite displacement capability of the rotary-shear machine, variations in perturbation magnitude and period were systematically explored (see also Chen et al., 2024). In the present study, we focus primarily on the effects of normal stress oscillations on fault behaviour and we explored three different distinct initial slip modes—stable sliding, fluctuating sliding, and stick-slipping—by systematically varying experimental conditions.

2.4. Data Acquisition and Processing

All transducer signals (devices highlighted in red in Figure 1a) were sampled at 30–900 Hz, while a separate acquisition system (Elsys) recorded the AE signals at 2 MHz and the torque couple data at 5 kHz.

Since the piston-sample assembly is fluid pressure compensated, the externally applied normal force on the gouge layer was directly calculated from the applied normal load and seal friction. Effective normal stress ($\sigma_n{}^e$) and shear stress (τ) were determined by assuming a uniform load distribution across the 3 mm annular width of the sample. The $\sigma_n{}^e$-value obtained included a correction for axial O-ring seal resistance of ~2.85 MPa. Additionally, the externally measured torque was corrected for dynamic seal friction, following displacement- and fluid pressure-dependent calibrations (Den Hartog et al., 2013). A standard error propagation analysis showed that $\delta\tau \leq 0.1\%$. During normal stress perturbation tests, seal friction in both shear and normal directions varied dynamically, but the effects were minor and not considered in this study.

Axial displacement L (reflecting gouge compaction/dilatation) was measured using the high-resolution LVDT (Figure 1a). During rapid $\sigma_n{}^e$-changes in the NSO tests with periods less than 1 s, L oscillated in phase with the imposed periodic forcing. Differentiating these measurements yielded the elastic stiffness (K_n) of the system in the axial (fault-normal) direction: $K_n = d(\sigma_n{}^e)/d(L)$. The obtained K_n value was used to correct L, thus allowing combined measurement of anelastic deformation and permanent changes in the gouge layer thickness (h) (Chen et al., 2024). A similar correction was applied to the Instron frame LVDT data, yielding consistent results with lower signal-to-noise ratios.

Using the torque data logged at 5 kHz, we were able to determine sample slip velocity (v_s) not only during stable sliding but also during fast slip events. This was done by analyzing shear deformation in a spring-slider system, incorporating the elastic coupling between shear and normal stress changes using the relation:

$$\dot{\tau} = K(v_{\text{imp}} - v_s) + \eta \cdot \dot{\sigma}_n^e. \tag{2}$$

Here K is the fault-shear stiffness, $\dot{\sigma}_n^e$ is the rate of change of normal stress (MPa/s), and η is a shear-normal stress coupling coefficient. The η-value was obtained from the above-mentioned fast NSO tests (i.e., with periods less than 1s), by means of a linear fit of the $\Delta\tau$ data to the applied oscillation amplitude ($2A$), yielding $\eta = d(\Delta\tau)/d(2A)$ (Chen et al., 2024). Removing the elastic coupling effect, the corrected shear stress (τ_{cor}) is given as:

$$\tau_{\text{cor}} = \tau - \eta\left(\sigma_n{}^e - \overline{\sigma}_n^e\right). \tag{3}$$

Using its time derivative, the sample slip rate (v_s) was then obtained from:

$$v_s = v_{\text{imp}} - \frac{\dot{\tau}_{\text{cor}}}{K} = v_{\text{imp}} - \frac{\dot{\tau} - \eta\dot{\sigma}_n{}^e}{K}. \tag{4}$$

Integrated displacement ($\Delta\delta_s$) over a time interval Δt was subsequently calculated as:

$$\Delta\delta_s = v_{\text{imp}} \cdot \Delta t - \frac{\Delta\tau_{\text{cor}}}{K} = v_{\text{imp}} \cdot \Delta t - \frac{\Delta\tau - \eta\Delta\sigma_n{}^e}{K}. \tag{5}$$

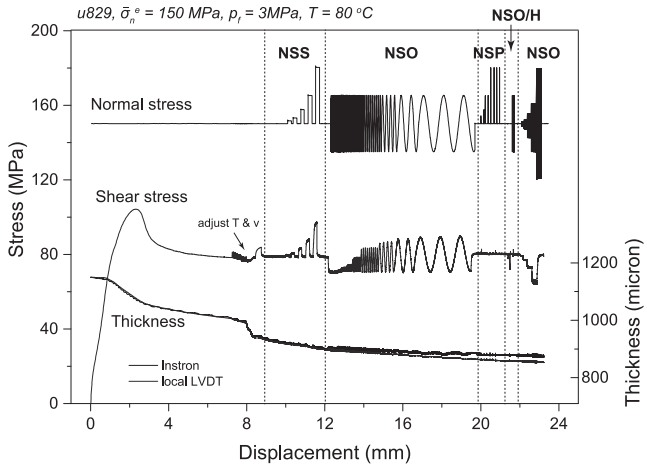

Figure 2. Results from a representative friction experiment (u829) on a simulated calcite gouge layer sheared under hydrothermal conditions ($\bar{\sigma}_n^e$ = 150 MPa, p_f = 3 MPa, T = 80°C, and v_{imp} = 1 μm/s), showing the variations of (effective) normal stress, shear stress, and corrected gouge layer thickness as a function of load-point displacement (u). The experiment composed of an initial loading, the temperature adjustments (from 120, 110, 100 to 80°C), and velocity step tests (between 10 and 1 μm/s), followed by different modes of normal stress variation tests: normal stress steps (NSS), normal stress pulses (NSP), normal stress oscillations (NSO) with varied amplitudes or frequencies, and NSO during a slide-hold-slide test (NSO/H) at 80°C and 1 μm/s. Note that the thickness is corrected for σ_n^e-variations using the fault-normal stiffness, while the large compaction at approximately ∼8 mm results from temperature adjustment, which effect remains uncorrected. Results from the NSP and NSO/H tests have been reported by Chen et al. (2024) and will not be covered in this study.

The stress drop and normal stress derivatives were computed using the Fast Fourier Transform (FFT) method. High-frequency noise was removed via low-pass filtering, with a cutoff frequency determined from the signal-noise spectral intercept.

The noise level of the reported AE measurements was systematically characterized as −60 dBV, estimated from a root-mean-square noise amplitude of ±1 mV (relative to a 1 V reference, calculated as dBV = 20 × $\log_{10}$ (0.001/1) = −60). This low noise level was achieved by switching to a manual fluid pump from the high-pressure servo-controlled pump: the latter introduced significant electronic interference, increasing noise to ∼−40 dBV (corresponding to an amplitude of ±10 mV).

Since the acoustic signals were occasionally affected by mechanical oscillations of the apparatus (i.e., during strong stick slips, and with a dominant natural frequency of ∼1 kHz), and by electronic pulse noises, acoustic emission events (AEs) were identified in the frequency domain. To achieve this, we performed Short-Time Fourier Transform analysis to the signal, using a 10-ms time window with a 5-ms overlap. AEs were automatically detected by setting a power spectral density (PSD) threshold at 150–300 kHz. The identified events were cross-validated against mechanically diagnosed slip events using Equation 4.

No absolute calibration of the PZT sensors was performed, and corrections for signal attenuation or source-receiver distance effects were not applied—consistent with common laboratory AE practices for relative event size comparisons (e.g., Colledge et al., 2023; Rivière et al., 2018). Because the geometry between the AE source (gouge layer) and receiver (PZT sensor) was fixed, and the source-receiver separation was large relative to the fault length (Figure 1), the peak AE amplitude (P) serves as a reliable measure of event size. Following prior laboratory AE studies (e.g., Colledge et al., 2023; Rivière et al., 2018), we use log(P) as a dimensionless proxy for relative event magnitude.

3. Results

3.1. General Results of a Representative Experiment

All the experiments showed a rapid, near-linear increase in shear stress during the first ∼0.6 mm of displacement, followed by apparent yielding and subsequent hardening, reaching the maximum strength at ∼2 mm displacement (Figure 2). As slip continued, the shear stress exhibited an exponential weakening to a steady level at a load-point displacement (u) of 6 mm, where the gouge showed either stable sliding (u574), small-amplitude fluctuations (u828 and u829), or stick slip (u589). Based on the basic behavior attained before imposing perturbations, this stage of each experiment is referred to as an "*initially stable*", "*-fluctuating*", and "*-stick-slipping*" test, respectively (Table 1). Subsequently, different modes of perturbations were applied to the normal stress with other parameters (p_f, T, and v_{imp}) maintained constant. The results of the experiments are given in Figure S1 of Supporting Information S1, showing the evolution of normal stress (σ_n), shear stress (τ), and corrected gouge layer thickness (h) versus load-point displacement.

Figure 2 presents an example of an *initially fluctuating* test, performed at $\bar{\sigma}_n^e$ = 150 MPa, T = 80°C, and p_f = 3 MPa (experiment u829). In this experiment, after a run-in of 7.0 mm displacement at 10 μm/s, we stepped the velocity (v_{imp}) to 1 μm/s and adjusted T from 120 to 80°C, from which we obtained an *initially fluctuating* behavior. Next, we started to perturb σ_n^e in different modes (i.e., NSS, NSP, and NSO) and continuously record the acoustic signals. The following sections only address the results from the NSS and NSO tests, as well as the accompanying AEs.

21699356, 2026, 5, Downloaded from https://agupubs.onlinelibrary.wiley.com/doi/10.1029/2025JB032273 by Tu Delft, Wiley Online Library on [27/05/2026]. See the Terms and Conditions (https://onlinelibrary.wiley.com/terms-and-conditions) on Wiley Online Library for rules of use; OA articles are governed by the applicable Creative Commons License

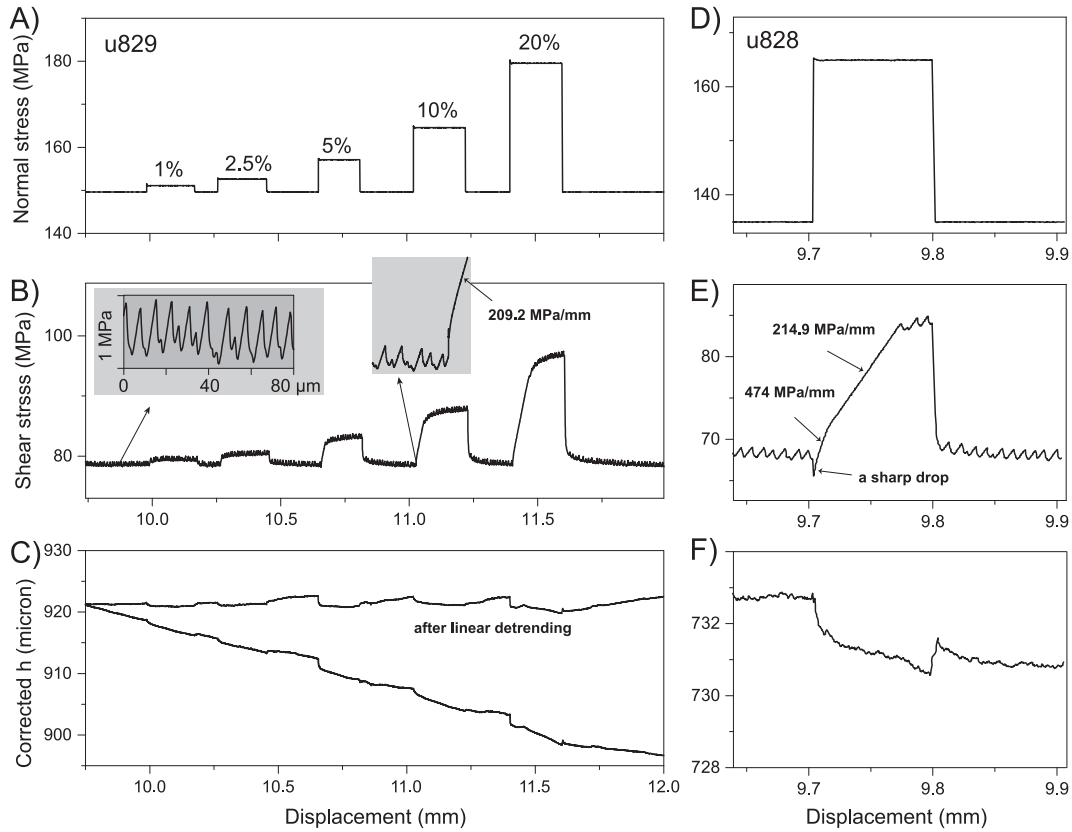

Figure 3. Typical results from normal stress stepping (NSS) tests, showing the evolution of normal stress, shear stress, and corrected gouge layer thickness (h) as a function of load-point displacement. Up-steps and down-steps were applied using the "Heaviside" control mode of the Instron frame (an embedded function for stepping test), with each step occurring within 0.2 s. Panels (a, b, and c) show results from experiment u829, performed at 80°C and 1 μm/s, with varying perturbation amplitudes (1%–20% of the base level $\overline{\sigma}_n^e$). Panels (d, e, and f) show resutls from experiment u828, performed at 100°C and 1 μm/s, with a 20% pertuabtion size. Prior to imposing the perturbations, the gouge exhibited self-sustained oscillations with periods of 6–13 s (u829) and 5–10 s (u828), respectivley.

3.2. Normal Stress Stepping (NSS) Tests

Figures 3a–3c illustrate typical results from a sequence of NSS tests sheared at 80°C (experiment u829). The shearing gouge initially showed small-amplitude fluctuations with irregular recurrent slip intervals of 6–15 μm (Figure 3b inset). In response to a (quasi)-instantaneous up-step in effective normal stress, the shear stress showed a small instantaneous increase, followed by a nearly linear increase corresponding to the elastic shear stiffness, and then by a gradual increase, at decreasing rate, to a new oscillation level. Following a down-step, the shear stress showed a rapid decrease and then gradually decreased to the original level.

Similar results were observed in the NSS experiment performed at 100°C (u828, Figures 3d–3f). In this case, in response to an up-step, the τ-evolution showed a small instantaneous decrease, followed by a rapid increase until reaching the long-range linear elastic stage (i.e., with a slope corresponding to elastic stiffness, Figure 3e). As slip proceeded, the shear stress abruptly transitioned toward a new mean level with superimposed small-amplitude oscillations (Figure 3e).

In both experiments, the thickness showed transient changes after the σ_n^e-steps (i.e., compaction following an up-step, and vice versa), with the evolution distance similar to that of the shear stress. The instantaneous and time-dependent contributions are asymmetric between up-steps and down-steps (cf. Figures 3c and 3f, see also Chen et al., 2024). The changes in gouge thickness increased with the amplitudes of the applied σ_n^e-steps (Figure 3c). The NSS results from other experiments, including one that initially exhibited stable-sliding behavior, are compiled in Figure S2 of Supporting Information S1.

21699356, 2026, 5, Downloaded from https://agupubs.onlinelibrary.wiley.com/doi/10.1029/2025JB032273 by Tu Delft, Wiley Online Library on [27/05/2026]. See the Terms and Conditions (https://onlinelibrary.wiley.com/terms-and-conditions) on Wiley Online Library for rules of use; OA articles are governed by the applicable Creative Commons License

21699356, 2026, 5, Downloaded from https://agupubs.onlinelibrary.wiley.com/doi/10.1029/2025JB032273 by Tu Delft, Wiley Online Library on [27/05/2026]. See the Terms and Conditions (https://onlinelibrary.wiley.com/terms-and-conditions) on Wiley Online Library for rules of use; OA articles are governed by the applicable Creative Commons License

3.3. Normal Stress Oscillation (NSO) Tests

In this study, oscillatory perturbations of normal stresses were applied in different friction regimes, where the gouges exhibited either stable sliding (u574), small-amplitude oscillation (u828 and u829), or stick-slip (u589) behaviors. In each case, we systematically varied the excitation period (t_{imp}) and/or amplitude ($2A$). The effect of load-point velocity (v_{imp}) was also investigated. Generally, the results of extracted parameters as a function of t_{imp} show a shift with v_{imp}, namely, increasing the load velocity causes a shift of the results to shorter excitation periods. This is consistent with previous results (e.g., Hong & Marone, 2005) and not the focus of the present study.

3.3.1. Effects of Excitation Period

Figure 4 presents the results from an oscillation test where the calcite gouge falls in the *v*-weakening regime and initially showed small-amplitude fluctuations with irregular time intervals, that is before $\sigma_n{}^e$ oscillations were applied. In this *initially fluctuating* test (u829), the sinusoidal variations of $\sigma_n{}^e$ were superimposed upon a base level ($\overline{\sigma}_n^e$) of 150 MPa with a fixed amplitude ($2A$ = 30 MPa, or 20% relative perturbation) and with different excitation periods (t_{imp}) from 0.4 to 1,000 s. When rapid oscillations were suddenly applied (t_{imp} = 0.4 s), a significant weakening by 10 MPa was observed in terms of the mean shear stress ($\overline{\tau}$) supported by the sample, that is, compared with the mean levels before the perturbation (see the shaded area in Figure 4a). Following Chen et al. (2024), this is referred to as "vibration-induced weakening." Removing the elastic coupling effect, the corrected gouge thickness showed a nominal dilatation by about 1 μm upon imposing the fast oscillations (Figure 4b). As t_{imp} increased, the amplitude of the resulting τ-variations ($\Delta\tau$) increased and the reduction in $\overline{\tau}$ decreased (Figure 4a). Generally, during short and long period ($t_{imp} \leq 5$ s or ≥ 200 s) oscillations, τ changed in phase with the externally applied $\sigma_n{}^e$, while in the intermediate periods (10–100 s), the τ-response became irregular in shape and showed delays in phase compared with the applied sinusoidal $\sigma_n{}^e$-variations (Figure 4c).

In the tests in which the gouge initially displayed stable sliding (u574), the behavior upon imposing oscillatory normal stresses was similar to that seen in the *initially fluctuating* tests. This includes the suppression of $\overline{\tau}$ upon suddenly imposing short-period $\sigma_n{}^e$-oscillations, and the irregular shape of τ-evolution and the double events within one cycle (or "period doubling") during intermediate periods (Figure S3 in Supporting Information S1).

In the tests in which the gouge initially exhibited stick slips (u589), subsequently oscillating the normal stress resulted in different effects compared with those described above. First, unlike in the *initially stable* or *-fluctuating* tests, imposing fast $\sigma_n{}^e$ oscillations did not lead to significant weakening. Figure 5 shows the results from a series of NSO tests that used increasing T (from 200 to 300°C) and $\overline{\sigma}_n^e$ (from 50 to 180 MPa). An increase in the T and $\overline{\sigma}_n^e$ resulted in increasingly unstable behavior of the fault, namely, from small-amplitude fluctuations to characteristic stick slips. Correspondingly, the τ-evolution, in response to the applied NSOs, showed a transition from one end-member to the other, namely, from (a) τ-variations with limited amplitudes and the same periods as the applied $\sigma_n{}^e$-oscillations (Figure 5a), to (b) enhanced stick slips, with recurrence times (t_r) and amplitudes ($\Delta\tau$) that were much larger than the characteristic values before the perturbations (t_r^{pre} and $\Delta\tau^{pre}$, Figure 5d). In the latter case (*end-member II*), the periodicity of the stick slips under perturbations did not correspond directly to the applied cycles of $\sigma_n{}^e$, although the overall curve was superimposed by small-amplitude, harmonic variations when the applied periods were short (<20 s).

At the condition that the gouge just began to exhibit stick-slip behavior (i.e., at the intermediate T and $\overline{\sigma}_n^e$, Figure 5b), the τ-evolution, in response to the applied NSOs, fell between the two end-members, depending on the excitation period. At the long periods ($\geq$10 s), the τ-evolution was strongly modulated by the $\sigma_n{}^e$ (*end-member I*); at the short periods ($\leq$1 s), the behavior showed characteristic cycles superimposed by small-amplitude vibrations (*end-member II*); at the intermediate periods (2–5 s), the responses interfered with the characteristic cycles, manifested by occasionally large-amplitude stress drops, with intervals comparable to the characteristic interval (see Figure 5b inset). With an increase in $\overline{\sigma}_n^e$ (Figure 5c), the behavior was closer to *end-member II*. The τ-evolution followed the rhythm of characteristic stick slips, albeit with enhanced stress drops occasionally (see the inset).

As observed in the *initially fluctuating* tests and reported in our previous studies (Chen et al., 2024; Yu et al., 2024), the sudden application of fast $\sigma_n{}^e$-oscillations resulted in a nominal anelastic dilatation of the gouge

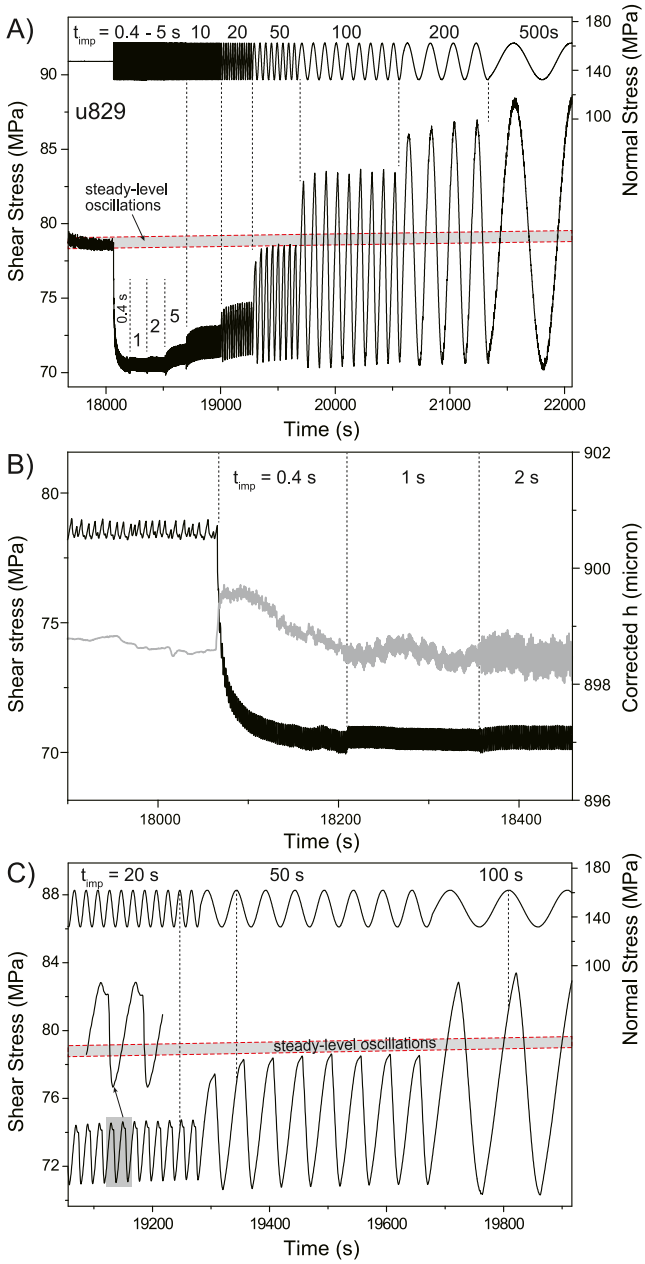

Figure 4. Evolution of shear stress under oscillating normal stresses on a calcite gouge that fell within the *v*-weakening regime and initially exhibited self-sustained oscillations prior to imposing the perturbations (experiment u829, performed at T of 80°C, v_{imp} of 1 μm/s and $\overline{\sigma}_n^e$ of 150 MPa). Panel (a) sinusoidal oscillations were applied with a fixed amplitude (2A = 30 MPa) and increasing oscillation periods (t_{imp}) from 0.4 to 1,000 s (only shown up to 500 s). Panel (b) blow-up of the short periods ($t_{imp} \leq 1$ s), where a nominal dilation of approximately 1 micron was observed upon the application of rapid normal stress oscillations. Panel (c) blow-up of the intermediate periods (t_{imp} = 20–100 s), where the shear stress cycles displayed a sawtooth-like shape with phase delay, indicated by the vertical dashed lines in (c).

layer, except that permanent compaction was observed when the gouge was first exposed to the highest $\overline{\sigma}_n^e$ (Figure S4 in Supporting Information S1). With the same perturbation amplitude ($2A = 5$ MPa), dilatation was measured to be 7–18 μm, and showed an increase with increasing T and $\overline{\sigma}_n^e$.

3.3.2. Effects of Excitation Amplitude

In the case of *initially fluctuating* tests, increasing the amplitude of normal stress vibrations ($2A$) of a fixed short period (c. 1 s) caused an increase in the amplitude of shear stress variations ($\Delta\tau$). As shown by Chen et al. (2024), $\Delta\tau$ and $2A$ follow a linear relation with a proportionality coefficient of 0.035 and near-zero intercept. We infer that this is due to the elastic coupling between shear stress and normal stress in the experimental configuration. As addressed earlier, we used this proportionality coefficient (η) to correct shear stress (Equation 2). As given by Chen et al. (2024), the magnitude of weakening (i.e., the reduction in mean shear stress) also follows a linear relation versus $2A$ with a slope of 0.256 and a relatively small intercept.

We further investigated the effect of vibration amplitudes on the stick-slip behavior under a fixed excitation period of 50 s. As shown in Figure 6, a decrease in the vibration amplitude resulted in smaller stress drops and shorter recurrence time. As revealed later by quantitative analysis, stick slip was strongly modulated by the imposed $\sigma_n{}^e$-perturbation: the timing of stick-slip events tended to be synchronous and the amplitudes were larger than expected assuming a constant friction ($2A\mu_{ss}$). This feature is distinct from the results obtained in the *initially stable* or *-fluctuating* tests.

3.4. Characteristics of Acoustic Emissions

It has been long recognized that carbonate deformation is generally quiet in terms of generating acoustic emissions (e.g., Trzeciak & Sone, 2021). This is supported by the fact that in the present experimental configuration, almost no events were detected during the initial stage of the two experiments instrumented with acoustic measurements (u828 and u829). Instead, acoustic emission events (AEs) were triggered later by imposing $\sigma_n{}^e$-perturbations. Figure 7a presents an example showing a burst of two tiny AEs, which are characterized by high power spectral density (PSD) between 150 and 350 kHz. In this example, the τ-curve displayed a distorted shape compared to the sinusoidal variations of normal stress applied. A rapid drop in shear stress occurred when $\sigma_n{}^e$ reached the maximum rate of decrease (cf. panels b1 and b2 of Figure 7b). As calculated from Equation 4, this corresponds to a pulse in the slip velocity which was about 5 times the load-point velocity ($v_\infty = 1$ μm/s). The two AEs occurred precisely during this slip pulse, with amplitudes that were 2–3 times the noise level (panel b3). A blow-up of the signals further showed that the two events were 15 ms apart, each lasting approximately 2 ms (panels b4–b5).

Imposing fast sinusoidal $\sigma_n{}^e$-oscillations did not generate any AE. However, imposing a "sawtooth" waveform caused a faster drop in shear stress and did generate AEs (Figures 8a–8c), though the amplitude of the event was small. The AEs were mostly triggered in NSS tests, by both up-steps and down-steps (Figures 8d–8i). As addressed earlier, in response to an up-step in $\sigma_n{}^e$, the shear stress first showed a small (<0.5 MPa) but rapid drop (<20 ms) before it started to increase (Figure 3e). The AEs induced upon the up-steps corresponded exactly to these small stress drops (Figure 8e, and see the generated waveforms in Figure S5 of Supporting Information S1). Figures 9a–9c present the AEs during a sequence of NSS tests (in experiment u828). Almost all the events detected

21699356, 2026, 5, Downloaded from https://agupubs.onlinelibrary.wiley.com/doi/10.1029/2025JB032273 by Tu Delft, Wiley Online Library on [27/05/2026]. See the Terms and Conditions (https://onlinelibrary.wiley.com/terms-and-conditions) on Wiley Online Library for rules of use; OA articles are governed by the applicable Creative Commons License

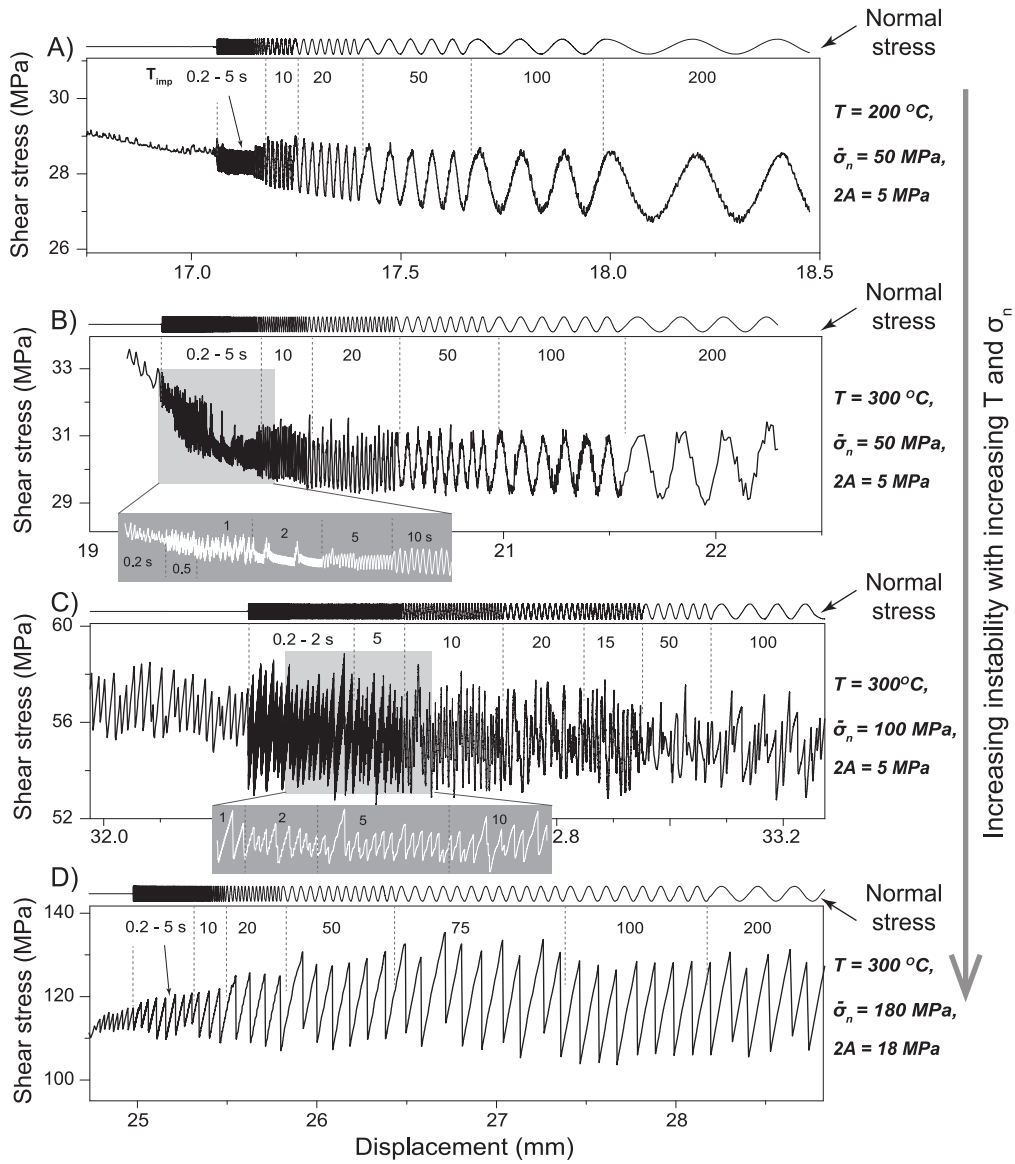

Figure 5. Shear stress evolution of a simulated calcite gouge in response to normal stress oscillations under five sets of T and $\overline{\sigma}_n{}^e$ conditions, where the gouge exhibited subtle fluctuations or stick slips prior to imposing the perturbations (experiment u589). Panels (a–d) show increasing T and $\overline{\sigma}_n{}^e$, which were used to amplify instability before applying the perturbations. As in Figure 4, sinusoidal perturbations were applied with increasing oscillation periods (i.e. from 0.2 to 500 s). All tests were conducted at a constant loading velocity of 1 μm/s.

corresponded with the $\sigma_n{}^e$-steps, and in most cases, multiple events were triggered by an individual step. Consistent with the example in Figure 8, the AEs were essentially associated with fast drops of shear stress, even in the upward steps. For the stepping tests analyzed (u828), the rate of decrease of shear stress, $|\dot{\tau}|$, ranged from 15 to 332 MPa/s (Figure 9b). Overall, the up-steps have larger $|\dot{\tau}|$-values than the down-steps, and in either direction, the values increased with increasing size of the $\sigma_n{}^e$-steps.

We found that the amplitudes of acoustic emission events varied systematically with the size of normal-stress steps (Figure 9c). As addressed earlier, we use $\log(P)$ as a dimensionless proxy for relative event magnitude—consistent with conventions for comparing event sizes in uncalibrated setups (e.g., Colledge et al., 2023; Rivière et al., 2018). When multiple AE events occurred during a single normal-stress step, we summed their logarithmic amplitudes ($\sum \log(P_i)$) to represent the total cumulative event size for that step. As shown in Figure 9d, this magnitude proxy is roughly proportional to the size of the $\sigma_n{}^e$-steps. Since the AEs were

21699356, 2026, 5, Downloaded from https://agupubs.onlinelibrary.wiley.com/doi/10.1029/2025JB032273 by Tu Delft, Wiley Online Library on [27/05/2026]. See the Terms and Conditions (https://onlinelibrary.wiley.com/terms-and-conditions) on Wiley Online Library for rules of use; OA articles are governed by the applicable Creative Commons License

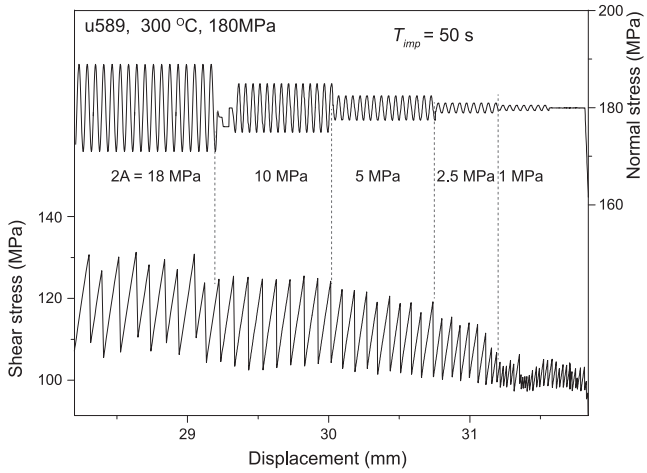

Figure 6. Shear stress evolution in response to normal stress oscillations with a 50 s period at $T = 300°C$, $v_{imp} = 1$ μm/s, and $\overline{\sigma}_n{}^e$ of 180 MPa (experiment u589), where the gouge exhibited typical stick slips prior to imposing the perturbations. Sinusoidal perturbations in normal stress were applied with a fixed period ($2A = 50$ s) and varying amplitudes.

presumably generated by (micro-)slip on the fault, we related $\sum \log(P_i)$ to the de-stressing rate $|\dot{\tau}|$. The results exhibited roughly linear relations for both up-steps and down-steps but with different slopes (Figure S6 in Supporting Information S1). From Equation 4, we further derived the slip rates associated with the stress drops. Adopting a K-value of 194 MPa/mm, a η-value of 0.035 (Chen et al., 2024), and assuming that the steps were completed within 10 ms (cf. The timescale of fast stress drops, Figure 8e), we obtained v_s ranging from 77 μm/s to 1.0 mm/s. Interestingly, the v_s-values resolved from up-steps and down-steps tend to merge and follow a linear relation with $\sum \log(P_i)$ (Figure 9e).

4. Quantifying the Frictional Response to Normal Stress Oscillations

Following Boettcher and Marone (2004) and Pignalberi et al. (2024), we now quantify the shear stress responses to the NSO tests. In the *initially stable* and *initially fluctuating* cases, we define four variables (Figure 10a): (a) amplitude of the shear stress variations (or stress drops), $\Delta\tau$; (b) the phase delay, $\Delta\Phi$, the phase difference between the peak in shear stress and the previous peak in normal stress normalized by the oscillation period (t_{imp}); (c) the failure phase, Φ_{fail}, the phase where the shear stress dropping rate reaches the minimum; and (d) the weakening, $\Delta\tau_w$, the difference in the mean shear stress ($\overline{\tau}$) before and during the $\sigma_n{}^e$-oscillations. Due to the observed nonlinear τ-response (e.g., period doubling), $\Delta\tau_w$ defined in the present study is different from the "yield strength" change ($\Delta\tau_y$) defined by Boettcher and Marone (2004), but they are interrelated via the relation: $\Delta\tau_y = \Delta\tau_w + \Delta\tau/2$. All phases are expressed in unit of radians.

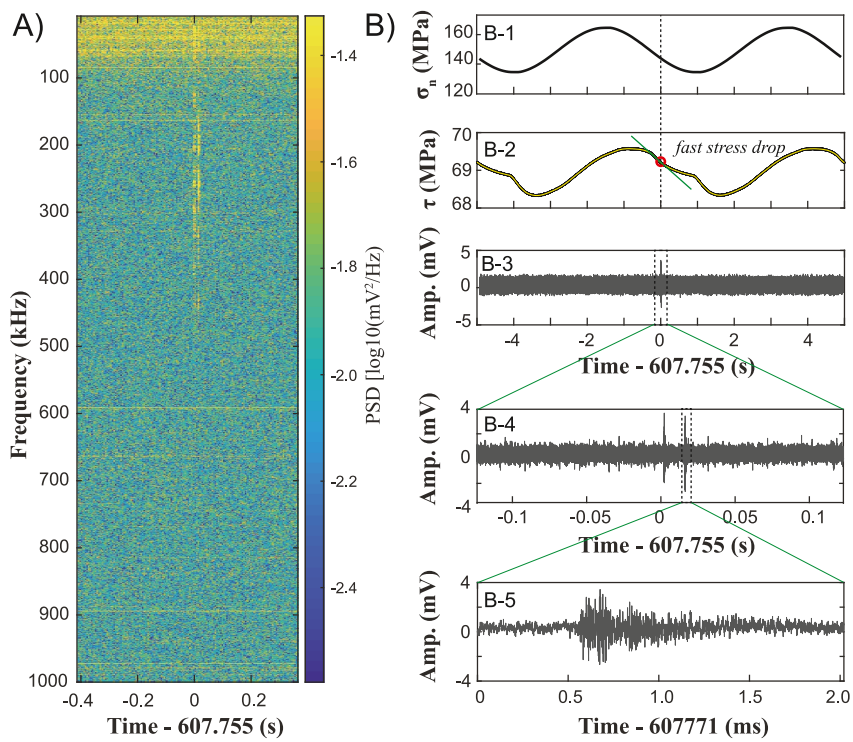

Figure 7. (a) Power spectrum density (PSD) of a 0.8 s acoustic signal, containing two small AE events that were potentially triggered by oscillating normal stress (experiment u829, performed under T of 80°C, $\overline{\sigma}_n{}^e$ of 150 MPa, and v_{imp} of 1 μm/s). Panel (b) the identified events are shown in five panels. B1—B3 present normal stress (σ_n), shear stress (τ), and the corresponding acoustic signal over a 10 s time window. B4 and B5) show blow-ups of the acoustic signal in time window of 0.2 s and 2 ms, respectively.

21699356, 2026, 5, Downloaded from https://agupubs.onlinelibrary.wiley.com/doi/10.1029/2025JB032273 by Tu Delft, Wiley Online Library on [27/05/2026]. See the Terms and Conditions (https://onlinelibrary.wiley.com/terms-and-conditions) on Wiley Online Library for rules of use; OA articles are governed by the applicable Creative Commons License

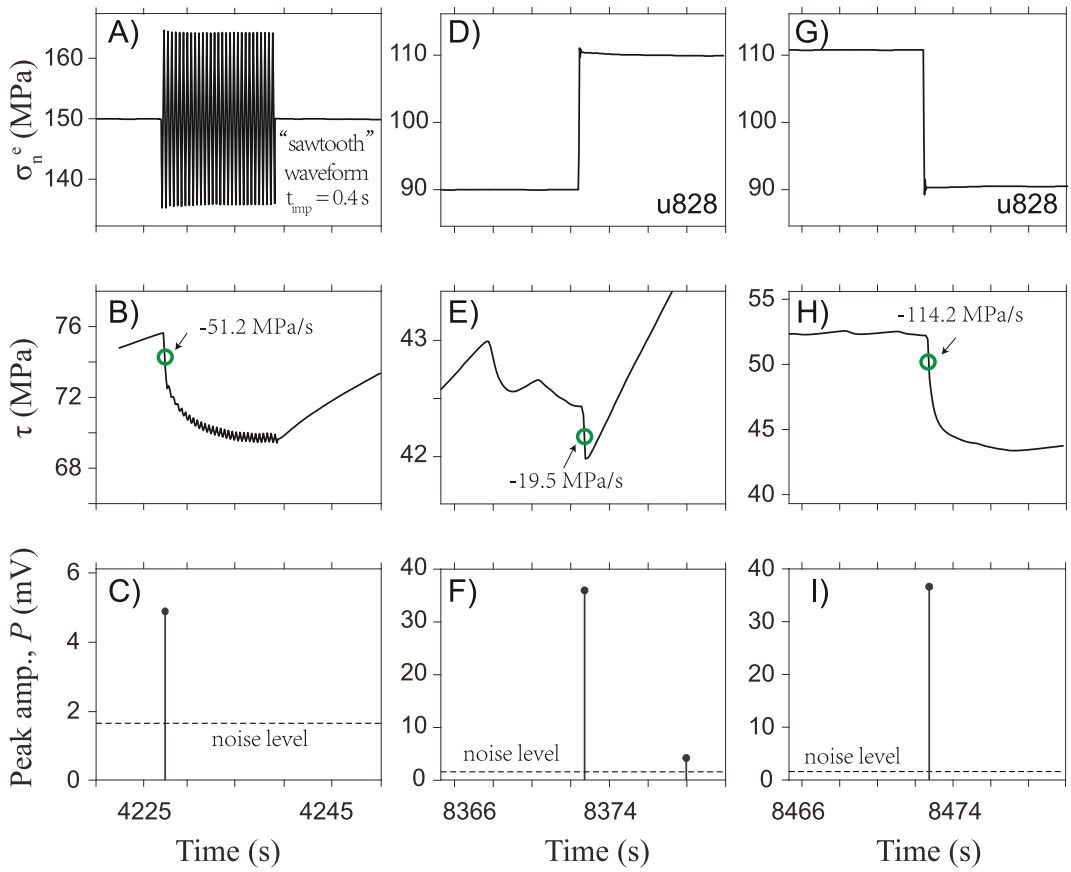

Figure 8. Normal stress, shear stress, and peak amplitude (amp.) of the picked AE events for a fast NSO test with a sawtooth waveform, along with upward and downward NSS tests (experimental u828, performed under T of 100°C, $\bar{\sigma}_n^e$ of 100 and 150 MPa, and v_{imp} of 1 μm/s)). Horizontal dashed lines indicate the noise level of approximately 1.6 mV. The results demonstrate that the AE events are consistently associated with rapid stress drops.

In the *initially stick-slipping* case, the gouge still exhibited stick slips after imposing NSOs. In this case, we determined $\Delta\tau$ and $\Delta\Phi$ (Figure 10b), and as addressed earlier, $\Delta\tau_w$ is nearly zero. Note that for stick-slip events, the peaks in shear stress were immediately followed by the failure (i.e., the times with the maximum rates of stress drop). Therefore, in the *initially stick-slipping* case, we have $\Phi_{fail} \sim \Delta\Phi$ (Figure 10b).

4.1. Results in the Initially Fluctuating Case

Figure 11 presents the effect of vibration period on shear strength in the *initially fluctuating* test, showing the stress drop ($\Delta\tau$), weakening ($\Delta\tau_w$) and phase lag ($\Delta\Phi$) as a function of t_{imp}. At short periods ($\lesssim$2 s), we observed a minimum $\Delta\tau$-value of 1 MPa and a maximum $\Delta\tau_w$-value of ~10 MPa. At long periods (>200 s), we observed a nearly zero weakening and the maximum $\Delta\tau$-value consistent with the expectation from the quasi-steady-state variations (Figure 11a). At intermediate periods, $\Delta\tau$ showed a monotonic increase and $\Delta\tau_w$, a decrease, with increasing t_{imp}. The onset of the changes in $\Delta\tau$ and $\Delta\tau_w$ fell in the periods of 5–20 s, which is consistent with the characteristic recurrence time seen before the perturbations (t_r^{pre}, see the shaded area). Interestingly, the slip rates (v_s) also showed the highest values in this period range.

Furthermore, as t_{imp} increased, $\Delta\Phi$ displayed a rise and then a decrease, with a maximum value of $\pi/2$ reached at 50 s period (Figure 11c). Similar results for $\Delta\tau$, $\Delta\tau_w$, and $\Delta\Phi$ were observed in the other test (Figure S7 in Supporting Information S1), except that a second cluster of $\Delta\Phi$ emerged from the doubling events. A final note here is that the sample slip rates (v_s) associated with these events were typically less than a few 10s-of-times the load-point velocity and the highest v_s-value obtained was less than 30 μm/s. Therefore, all the events induced are considered to be slow.

21699356, 2026, 5, Downloaded from https://agupubs.onlinelibrary.wiley.com/doi/10.1029/2025JB032273 by Tu Delft, Wiley Online Library on [27/05/2026]. See the Terms and Conditions (https://onlinelibrary.wiley.com/terms-and-conditions) on Wiley Online Library for rules of use; OA articles are governed by the applicable Creative Commons License

21699356, 2026, 5, Downloaded from https://agupubs.onlinelibrary.wiley.com/doi/10.1029/2025JB032273 by Tu Delft, Wiley Online Library on [27/05/2026]. See the Terms and Conditions (https://onlinelibrary.wiley.com/terms-and-conditions) on Wiley Online Library for rules of use; OA articles are governed by the applicable Creative Commons License

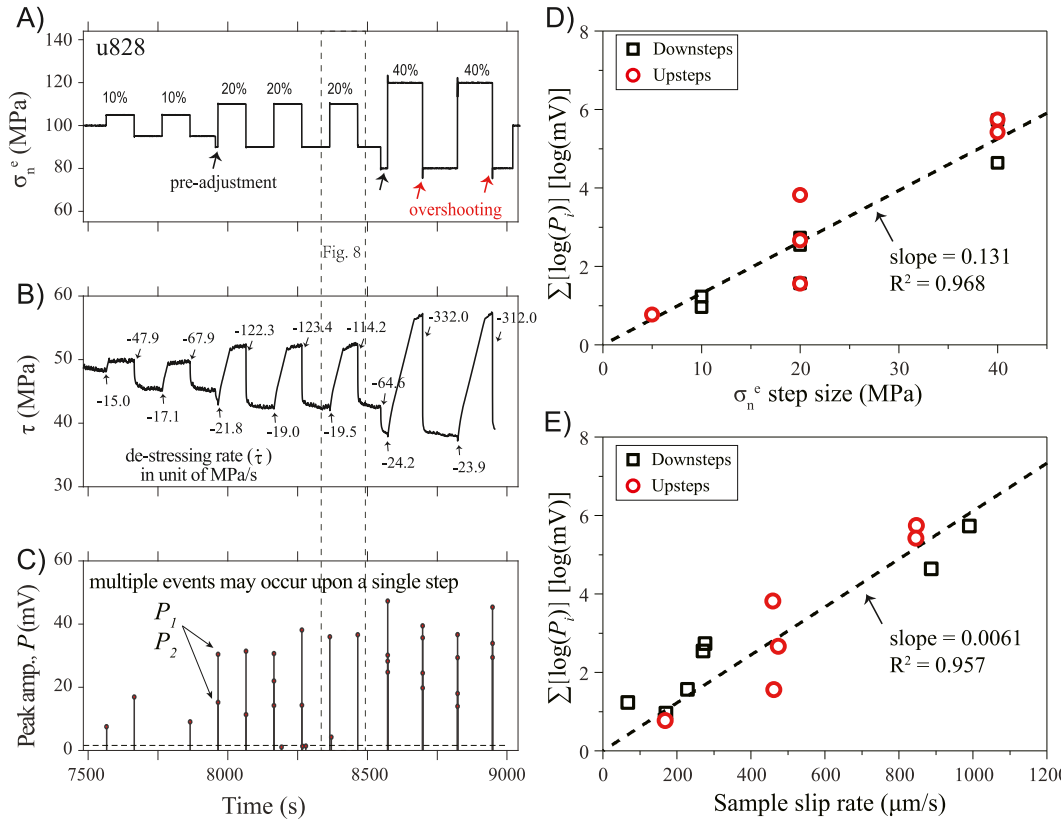

Figure 9. Characteristics of the triggered AE events in response to different size in perturbation of effective normal stress and the resulting shear stress drops and slip rates (experimental u828, in the phase of tests performed under T of 100°C, $\bar{\sigma}_n^e$ of 100 MPa, and v_{imp} of 1 μm/s). Panel (a) effective normal stress, (b) shear stress, and (c) peak amplitude (amp.) of the picked AE events as a function of time in a sequence of NSS tests. The rate of shear stress drop for each step is labeled in (b). The multiple dots in (c) represent bursts of multiple events during one step. The dashed area highlights the upward and downward NSS tests shown in Figure 8. Using $\sum \log(P_i)$ as a substitute, the local seismic magnitudes show linear relationships to (d) the step sizes of effective normal stress, and (e) the sample slip rates associated with drops in shear stress.

4.2. Results in the Initially Sticking-Slipping Case

In the case that the gouge initially exhibited stick-slip behavior (u589), the τ-response showed markedly enhanced stick-slip events compared with the pre-existing ones, which had amplitudes of less than 4 MPa and recurrence periods of 10–35 s. The overall dependence of $\Delta\tau$ on the oscillation period (t_{imp}) resembles the trends described above (Figure 12a). At short periods (≤2 s), $\Delta\tau$ reaches a minimum; as t_{imp} increases, $\Delta\tau$ increases and then retains a high level at long periods (≥100 s). Because the excitation period applied was still limited (≤500 s), it remains uncertain whether $\Delta\tau$ saturated at this high level or would decrease again at even longer periods. Interestingly, during the intermediate periods (2–100 s), $\Delta\tau$ follows a roughly log-linear relation versus t_{imp}. As in the other experiments, the maximum v_s-value is reached within this intermediate-period domain.

Our results further showed that the $\Delta\tau$-values of the stick-slip events increase with $2A$, also following a more or less log-linear relation (Figure 12b and the inset). Due to the low logging rate used in the experiment, the v_s-values were systematically underestimated. A key point here is that $\Delta\tau$-values obtained here are much higher than the value expected from the quasi-steady-state variations ($2A\mu_{ss}$), especially when t_{imp} is greater than t_r^{pre} (Figure 12a).

4.3. Failure Phases in Both Cases

Phase analysis revealed that at short (≤2 s) and long (≥100 s) excitation periods, the "failure phases" (Φ_{fail}) are around 0.5π in the *initially fluctuating* tests (Figure 13a and Figure S8 in Supporting Information S1), since shear stress changed almost in phase with σ_n^e. In the intermediate periods (2 s < t_{imp} < 100 s), the Φ_{fail}-values increase

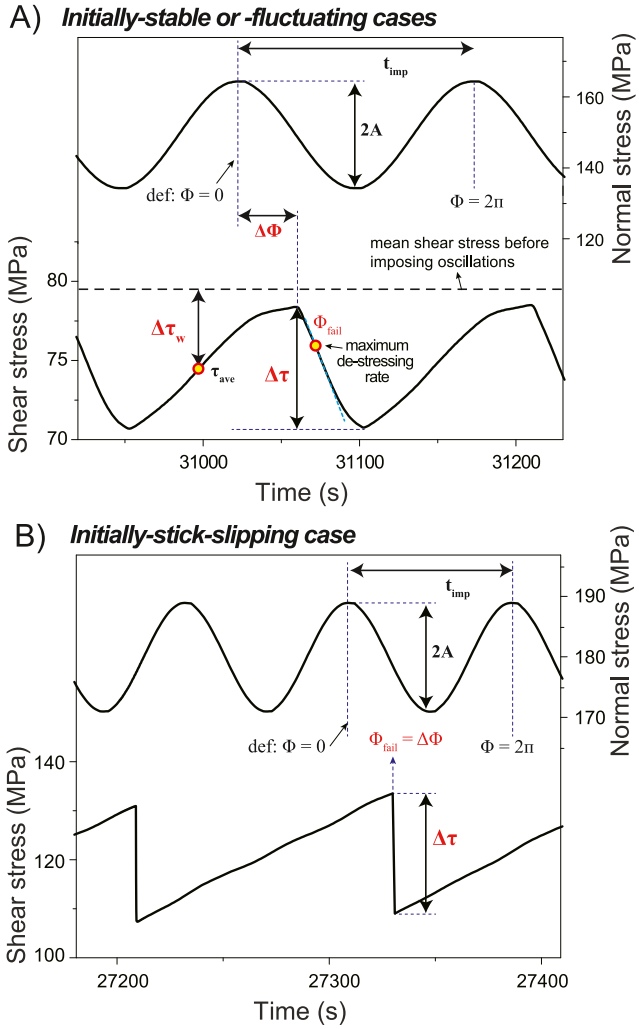

Figure 10. Definition of frictional parameters for normal stress oscillation tests, including $\Delta\tau$, $\Delta\tau_w$, $\Delta\Phi$ and Φ_{fail}, in the (a) *initially stable* or -*fluctuating* cases, and (b) *initially stick-slipping* tests. The phase (Φ) is defined following Schuster's method (1987), where $\Phi = 0$ and 2π correspond to consecutive peaks in effective normal stress (σ_n^e). See the text for detailed definitions. The examples shown in (a, b) are from experiment u829 and u589, respectively.

and fall between 0.5π and 1π (Figure 12a and the inset). Note that in the case of doubling, there is a second failure phase at around 1.75π (Figure S8 in Supporting Information S1).

The same range of phases prone to failure (0.5π–1π) was also seen in the *initially stick-slipping* tests, with a prominent peak phase at $\sim 0.75\pi$ (Figure 13b). This peak becomes more evident when the results were only derived from the intermediate periods (2–100 s), where the instability was enhanced, resulting in events of larger stress drops and slip rates.

5. Discussion

In this study, we conducted σ_n^e-perturbation tests on simulated carbonate fault gouges under specific hydrothermal conditions, where friction fell within the *v*-neutral to *v*-weakening regime and the gouge exhibited either stable sliding, small-amplitude fluctuations, or stick-slip behavior prior to perturbation. In the following discussion, we highlight several new observations from our experiments, including (a) slow and aseismic slip induced by exerting fast vibrations on *initially stable or -fluctuating* faults, and (b) enhanced instability of *initially stick-slipping* faults by exerting vibrations at specific ranges of period. We focus primarily on these key phenomena and comparisons with previous studies, most of which were conducted at room temperature, exhibiting initially stable sliding behavior. We also discuss the responsible mechanisms and implications of these findings for both natural and induced seismicity. The theoretical developments needed to explain these normal stress effects will be addressed in future work.

5.1. Slow and Aseismic Slip Induced by Fast Vibrations

5.1.1. A Stabilizing Effect and Possible Mechanism(s)

Our experiments under *initially stable* and *-fluctuating* conditions indicate that short-period vibrations induce weakening (Figure 4b and Figure S3 in Supporting Information S1). We observed a significant shear strength reduction of up to 10 MPa (~10%), which is notably higher than that reported for quartz gouges at room temperature (Boettcher & Marone, 2004). Vibration-induced weakening has also been observed in both granular and solid friction systems under dry and wet conditions (e.g., Bureau et al., 2000; Capozza et al., 2009; Chen et al., 2024; Dang et al., 2018; Heuberger et al., 1998; Pignalberi et al., 2024).

As shown in the shear stress curve after correcting for elastic coupling, short-period oscillations not only induce weakening but also stabilize slip by eliminating the original shear stress fluctuations (yellow line in Figure 14a, u829). We note that the magnitude of weakening (~10 MPa) and the induced shear displacement (57 μm, Figure 14b) are comparable to those of typical stick-slip events (cf. Figure 5d). However, the maximum displacement rate, calculated from Equation 4 using shear stiffness of 188 MPa/mm and coupling coefficient (η) of 0.031, was only ~16 μm/s — substantially lower than that of typical stick-slip events. A similar phenomenon was observed in tests with fast "sawtooth" waveforms rather than sinusoidal vibrations (Figure S9 in Supporting Information S1). This slow-slip behavior is further supported by the acoustic measurements, which detected minimal acoustic signals during the oscillation tests (Figure 14c). These observations suggest that rapid σ_n^e-vibrations can suppress original instability (if present) and promote slow rather than fast fault slip, implying a stabilizing effect.

Stabilization by external vibrations has previously been reported in laboratory experiments on geo-materials and lubricants, including glass beads and polymers (Bureau et al., 2000; Capozza et al., 2011; Cochard et al., 2003; Lastakowski et al., 2015; Vidal et al., 2019), as well as in numerical studies using discrete element and molecular dynamic simulations (e.g., Ferdowsi et al., 2015; Gao et al., 1998; Griffa et al., 2013; Guerra et al., 2008;

21699356, 2026, 5, Downloaded from https://agupubs.onlinelibrary.wiley.com/doi/10.1029/2025JB032273 by Tu Delft, Wiley Online Library on [27/05/2026]. See the Terms and Conditions (https://onlinelibrary.wiley.com/terms-and-conditions) on Wiley Online Library for rules of use; OA articles are governed by the applicable Creative Commons License

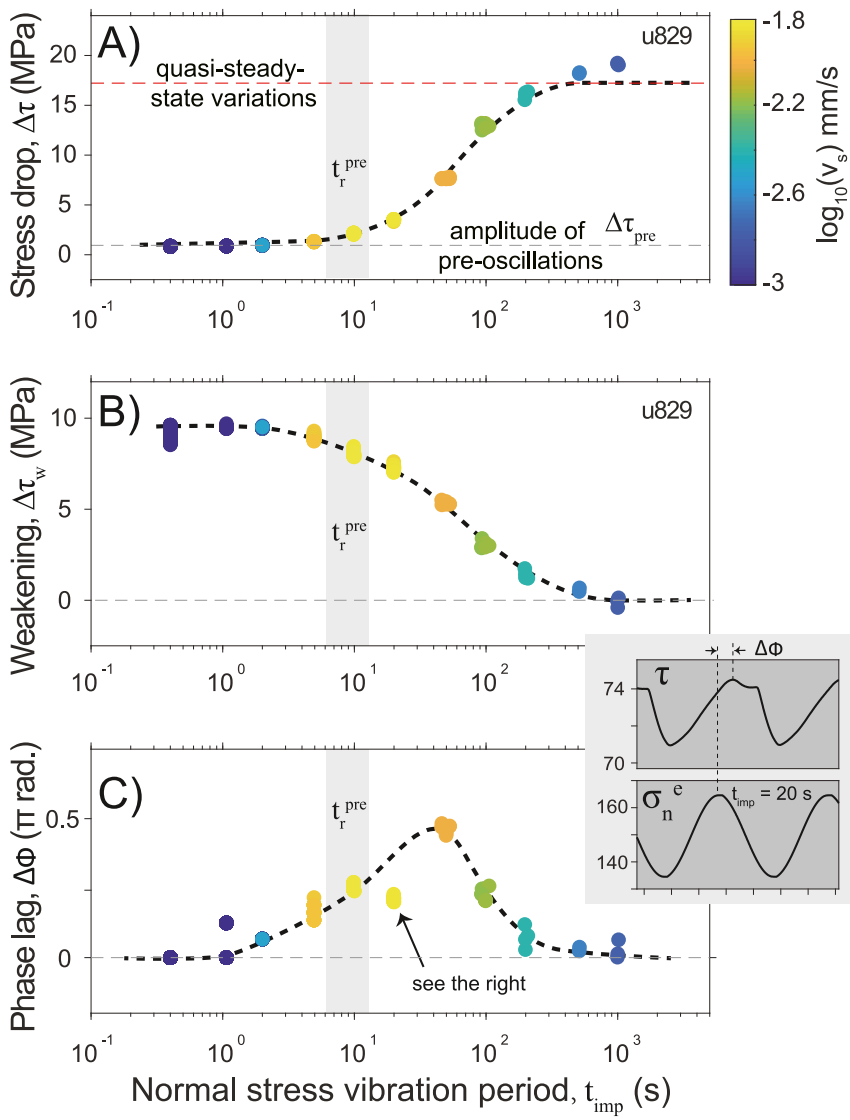

Figure 11. Effect of normal stress vibration period on frictional strength of an *initially fluctuating* fault (experiment u829, performed under T of 80°C, $\bar{\sigma}_n^e$ of 150 MPa, and v_{imp} of 1 μm/s). Panel (a) stress drop ($\Delta\tau$), (b) weakening ($\Delta\tau_w$), and (c) phase lag ($\Delta\Phi$) as functions of normal stress vibration periods (t_{imp}) ranging from 0.4 to 1,000 s. The experiment was conducted at v_{imp} = 1 μm/s, T = 80°C, and $\bar{\sigma}_n^e$ of 150 MPa, where the shear stress initially exhibited self-sustained fluctuations with a characteristic recurrence period (t_r^{pre}) of 6–15 s (grey shaded area) and an amplitude of 1 MPa (grey dashed line in a). Sinusoidal perturbations were applied with a constant peak-trough amplitude (2A) of 30 MPa. The expected quasi-steady-state change in shear stress ($2A\mu_{ss}$) is shown in (a), assuming a nominal steady-state friction (μ_{ss}) of 0.6. The thick dashed lines highlight estimated trends of t_{imp}. Circular symbols are color-coded by peak sample slip velocities (v_s) during stress drops, with a maximum v_s of ~30 μm/s occurring when t_{imp} is close to t_r^{pre}.

Thompson & Grest, 1991). However, the underlying mechanisms governing slip induced by short-term variations and the evolution of fault strength remain poorly understood. One possible explanation is acoustic fluidization, a mechanism well established in undrained granular systems (Melosh, 1979). Alternative interpretations, based on laboratory and numerical experiments, include self-fluidization (Wortel et al., 2016), contact opening (Ferdowsi et al., 2015), grain-contact nonlinearity, and surface roughness effects (Lastakowski et al., 2015; Vidal et al., 2019). Our recent results suggest that fast vibrations may induce nominal dilatation (Chen et al., 2024), a phenomenon also observed in this study (Figure 4b and Figure S4 in Supporting Information S1). This finding aligns with the numerical studies indicating that rapid vibrations promote contact opening and a reduction in

21699356, 2026, 5, Downloaded from https://agupubs.onlinelibrary.wiley.com/doi/10.1029/2025JB032273 by Tu Delft, Wiley Online Library on [27/05/2026]. See the Terms and Conditions (https://onlinelibrary.wiley.com/terms-and-conditions) on Wiley Online Library for rules of use; OA articles are governed by the applicable Creative Commons License

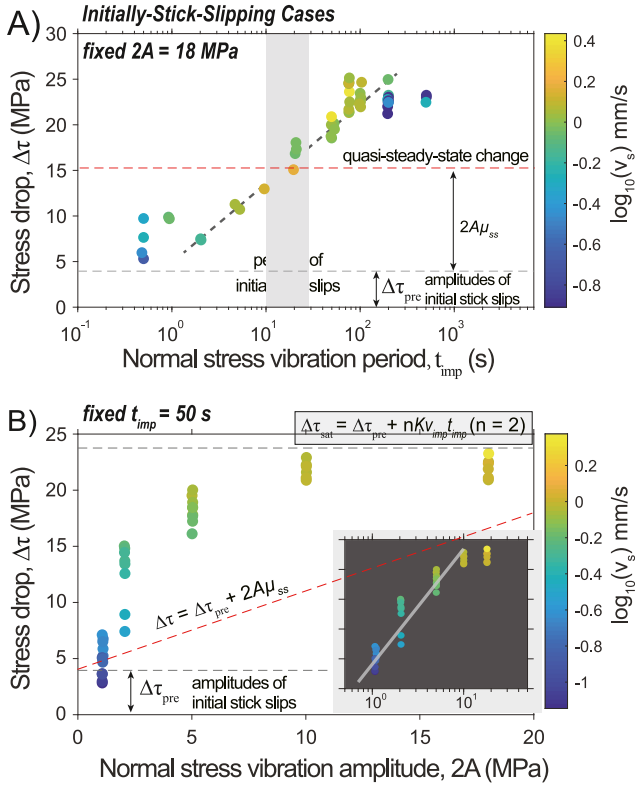

Figure 12. Effect of normal stress vibration period and amplitude on frictional strength of an *initially stick-slipping* fault (experimental u589, in the phase of testes performed under T of 300°C, $\overline{\sigma}_n^e$ of 180 MPa, and v_{imp} of 1 μm/s). Stress drop of stick slips ($\Delta\tau$) as a function of (a) the excitation period (t_{imp}) with a fixed excitation amplitude ($2A = 18$ MPa), and (b) of the excitation amplitude ($2A$) with a fixed excitation period ($t_{\text{imp}} = 50$ s). The pre-perturbation stick slips exhibit characteristic periods of 10–35 s, shown in the shaded area in (a). In the inset of (b), the same $\Delta\tau$ values are plotted against the logarithm of $2A$. In both graphs, characteristic stress drops of 4 MPa are indicated by dashed lines, and quasi-steady-state changes ($2A\mu_{ss}$) are added, assuming a steady-state friction (μ_{ss}) of 0.67. The symbols are color-coded by the maximum slip velocity during stress drops. Due to the experiment's sampling rate of 100 Hz, the measured maximum velocity (v_s) is artificially limited to ~2 mm/s.

coordination number (Ferdowsi et al., 2015; Zaloj et al., 1999), and is further supported by small-scale surface friction experiments on lubricants (Heuberger et al., 1998).

5.1.2. Characteristic Time Scales and How Fast Need the Excitation Be?

A key question is: How fast must vibrations be to induce weakening while maintaining slow, and stable deformation? As discussed earlier, when the vibration period approaches or slightly exceeds the recurrence period observed before perturbation (t_r^{pre}), cyclic loading can enhance instability, leading to events with larger stress drops and higher slip rates. Therefore, to induce slow weakening, the excitation periods must be shorter than t_r^{pre}. Meanwhile, our results indicate a lower bound in the vibration period (t_{sat}), below which weakening tends to saturate (e.g., <2 s in Figure 11b, <0.5 s in Figure S7 of Supporting Information S1). The saturation period is generally a few times shorter than t_r^{pre} (Figure 11 and Figure S7 in Supporting Information S1).

These two periods likely correspond to two intrinsic timescales of the simulated fault system. In the framework of classical RSF, the timescale characterizing state evolution under small perturbation is

$$t^c = \frac{D_c}{v_{\text{imp}}}, \tag{6}$$

where D_c is the characteristic slip distance and v_{imp} is the imposed loading velocity. The characteristic recurrence time (t_r^c) associated with self-sustained oscillations is given by Rice and Ruina (1983); Ruina (1983):

$$t_r^c = 2\pi \frac{D_c}{v_{\text{imp}}} \sqrt{\frac{a}{b-a}}, \tag{7}$$

where a and b are the rate-and-state friction parameters for the direct and evolution effect, respectively. It can be readily shown that t_r^c is typically greater than t^c. Sustained oscillations occur when the shear stiffness (K) equals the critical stiffness ($K_c = \sigma_n^e(b-a)/D_c$). As shear stiffness decreases, the instability strengthens and the recurrence time increases. Therefore, t_r^c represents the minimum recurrence time of the fault system, that is, $t_r^c \le t_r^{\text{pre}}$. Given RSF parameters of the same gouges at 80–100°C ($a = 0.006$, $b = 0.009$, $D_c = 1$–5 μm, Chen et al., 2015), and $v_{\text{imp}} = 1$ μm/s, the estimated t^c and t_r^c are 1–5 s and 9–45 s, respectively. These values are broadly consistent with the observed pre-perturbation recurrence times and saturation periods for oscillation-induced weakening. We therefore propose that, to induce slow weakening, the excitation period should be significantly shorter than t_r^c, and, conservatively, shorter than t^c.

Beyond the excitation period, vibration-shear experiments suggest that the governing parameter for frictional weakening and stability transition (i.e., from unstable to stable sliding), is the characteristic velocity of the imposed vibrations, given as $2A/t_{\text{imp}}$, the combination of vibration period and amplitude (Lastakowski et al., 2015; Vidal et al., 2019). This viewpoint is supported by more recent experiments which demonstrate a linear relationship between weakening and vibration amplitude (Chen et al., 2024; Yu et al., 2024). Addressing these questions requires sophisticated theoretical and numerical investigations incorporating an appropriate constitutive friction law (e.g., Barbot, 2024; Barbot et al., 2025; Chen, Niemeijer, & Spiers, 2025; Linker & Dieterich, 1992; Pignalberi et al., 2024; Shreedharan et al., 2019).

21699356, 2026, 5, Downloaded from https://agupubs.onlinelibrary.wiley.com/doi/10.1029/2025JB032273 by Tu Delft, Wiley Online Library on [27/05/2026]. See the Terms and Conditions (https://onlinelibrary.wiley.com/terms-and-conditions) on Wiley Online Library for rules of use; OA articles are governed by the applicable Creative Commons License

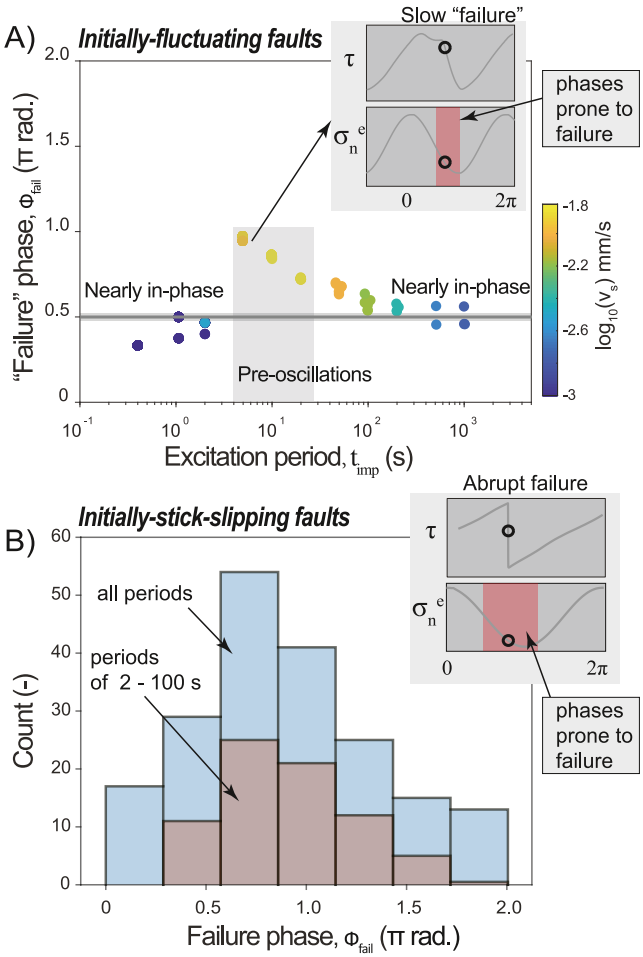

Figure 13. Failure phases in response to normal stress variations. Panel (a) failure time as a function of oscillation period in an *initially fluctuating* fault (data from experiment u829, performed at T of 80°C, $\overline{\sigma}_n^e$ of 150 MPa, and v_{imp} of 1 μm/s); (b) Histogram of failure times in an *initially stick-slipping* fault (data from experiment u589, including three phases conducted at T of 300°C, and $\overline{\sigma}_n^e$ of 50, 100, and 180 MPa, respectively). Insets show typical shear and normal stress cycles in the intermediate-period domain, where frictional instability was enhanced.

5.2. Fault Instability Reinforced and Modulated by Normal Stress Vibrations

5.2.1. Enhanced Instability at Specific Excitation Periods

Under *initially fluctuating* conditions, the shear stress (τ) response was strongly influenced by oscillatory normal stress perturbations, leading to characteristic "doubling" and irregular stress variations (Figure 4 and Figure S3 in Supporting Information S1), along with significant weakening and phase delays (Figure 11). This phenomenon primarily occurred when the excitation period was close to the recurrence time before perturbation ($\sim t_r^{pre}$), and the resulting slip velocities remained relatively low, indicative of slow-slip events (Figure 11). These observations generally align with previous experiments (see Figure 6 of Yu et al., 2024; Figure 8 of Pignalberi et al., 2024) and theoretical predictions within the RSF framework (Boettcher & Marone, 2004; Pignalberi et al., 2024).

In contrast, when normal stress perturbations were applied to an *initially stick-slipping* fault, instability was significantly enhanced. This was characterized by larger stress drops ($\Delta\tau > \Delta\tau^{pre}$, Figure 5d) and faster slip rates (Figure 12). The periods that most effectively enhanced instability spanned a broad range, from several times shorter to orders of magnitude longer than t_r^{pre}. This range was wider than that observed in the *initially fluctuating* (cf. Figures 11 and 12) or *initially stable* cases (Figure S7 in Supporting Information S1). Additionally, in the *initially stick-slipping* case, the amplitudes of stress drops under perturbations greatly exceeded the one expected assuming a constant steady-state friction ($2A\mu_{ss}$), and retained at a high level when $t_{imp} > t_r^{pre}$ (Figure 12a). This differs from previous experiments on bare rock surfaces and fault gouges at room temperature, where τ-variations were generally lower than or equal to $2A\mu_{ss}$ (e.g., Bartlow et al., 2012; Boettcher & Marone, 2004; Huang et al., 2016; Lockner & Beeler, 1999).

We found that the increase in stress drops ($\Delta\tau$) followed a log-linear relation with the imposed perturbation amplitude and ultimately reached a saturation level (Figure 12b, inset). This saturation level likely results from stress accumulation over an integer multiple of the excitation period (t_{imp}). In our experiments, the integer n was found to be equal to or less than 2 (Figure 10b), leading to a saturation of stress drop:

$$\Delta\tau_{sat} = \Delta\tau_{pre} + n \cdot (K v_{imp} t_{imp}), \quad (8)$$

where $\Delta\tau_{pre}$ is the amplitude of pre-perturbation events (~4 MPa), v_{imp} = 1 μm/s, t_{imp} = 50 s, and K = 200 MPa/mm (Figure 6). Substituting these values yields $\Delta\tau_{sat}$ of 24 MPa, which closely matches our experimental observation (Figure 12b).

Theoretical studies suggest that enhanced sensitivity with $\Delta\tau > 2A\mu_{ss}$ occurs when resonance conditions are met in v-weakening faults (Perfettini et al., 2001; Perfettini & Schmittbuhl, 2001). These conditions are highly restrictive, requiring: (a) a relative stiffness $K/K_c < 1.1$, and (b) an excitation period t_{imp} close to the critical recurrence time (i.e., 0.5–2 times), and (c) a perturbation size $A/\overline{\sigma}_n^e$ above a friction parameter-dependent threshold (Perfettini et al., 2001, Equation 46). Compared to these theoretical results, our experiments revealed a much broader range of sensitive periods (Figure 12a). While we did not systematically investigate the effect of perturbation size, our results suggest that a perturbation of 0.6% is sufficient to enhance instability (Figure 12b). Additionally, while previous theory (Perfettini et al., 2001) predicts resonance behavior at near critical conditions ($K/K_c \approx$ (a), our results indicate that resonance may occur at lower stiffness ratios (cf. The four cases in Figure 5).

21699356, 2026, 5, Downloaded from https://agupubs.onlinelibrary.wiley.com/doi/10.1029/2025JB032273 by Tu Delft, Wiley Online Library on [27/05/2026]. See the Terms and Conditions (https://onlinelibrary.wiley.com/terms-and-conditions) on Wiley Online Library for rules of use; OA articles are governed by the applicable Creative Commons License

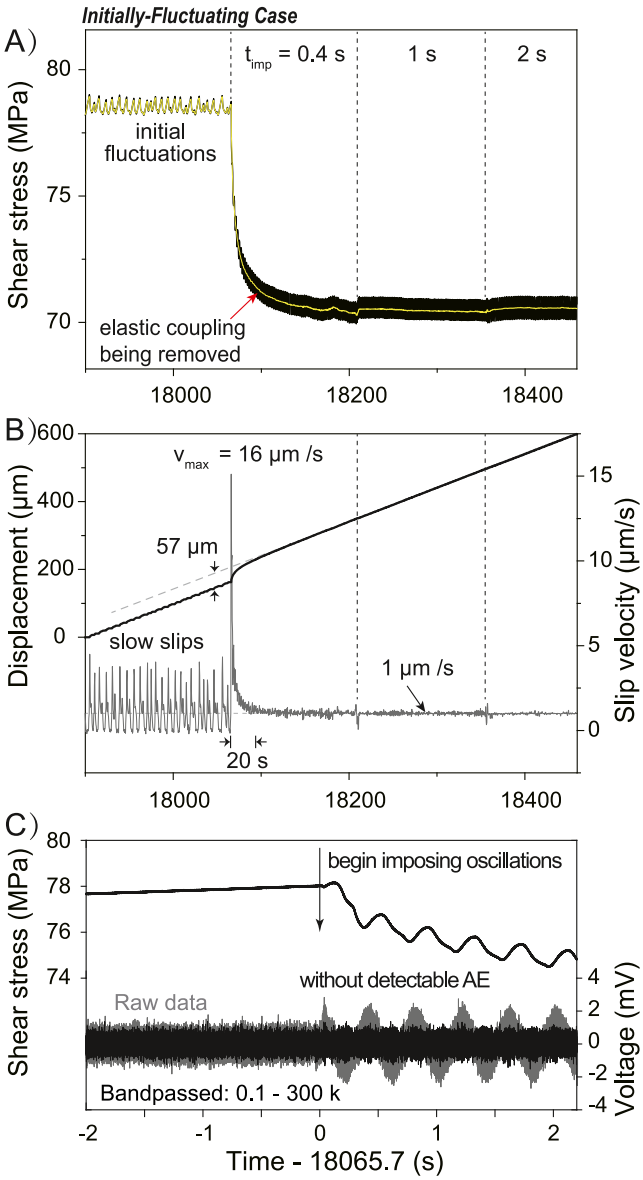

Figure 14. Generation of aseismic slip by imposing fast oscillations. Panel (a) shear stress evolution (as in Figure 4b), with the corrected shear stress after removing the elastic coupling to normal stress shown in yellow. Panel (b) resolved sample shear displacement and velocity. Panel (c) zoom-in view of shear stress and acoustic data.

Overall, we observed significantly enhanced instability under hydrothermal conditions, with effects being more pronounced at higher temperatures —an outcome rarely reported in previous studies (Boettcher & Marone, 2004). We suspect this discrepancy arises because most prior experiments were conducted at room temperature. To confirm this, future experiments should systemically explore other materials and the effects of variations in t_{imp}, $A/\overline{\sigma}_n^e$ and K/K_c. Furthermore, theoretical studies on stress modulation under inherently unstable conditions ($K < K_c$) remain lacking (Ader et al., 2012; Putelat et al., 2012).

5.2.2. Triggering and Synchronization of Unstable Events

Another key observation is that normal stress oscillations modulated the timing of unstable events. Specifically, failure events predominately occurred within the phase range from 0.5π to 1.0π (Figure 13). The phase of 1.0π corresponds to the minimum of the oscillating σ_n^e, where failure likely follows a threshold-type model such as Mohr-Coulomb failure (Lockner & Beeler, 1999). In contrast, failure at 0.5π coincides with the peak de-stressing rate, consistent with weakening controlled by the rate of stress change (Beeler & Lockner, 2003). The synchronization of stick-slip events has been widely reported in previous experiments performed under varying normal stress or fluid pressure conditions (e.g., Chelidze & Matcharashvili, 2013; Lockner & Beeler, 1999; Savage & Marone, 2007). The results from these previous studies generally supported failure correlating with minimum normal stress ($\Phi_{\mathrm{fail}} \sim 1.0\pi$). Recent experiments using cyclic loading have mainly focused on anthropogenic seismicity, such as fluid injection-induced seismicity. For instance, Chanard et al. (2019) and Noël, Pimienta, and Violay (2019) observed peak seismicity during the low-pressure phase of the cycle, consistent with the threshold stress failure model. Similarly, Wang, Kwiatek, Rybacki, Bonnelye, et al. (2020) reported failure phases of 0.5π−1.0π in experiments with monotonic fluid pressure changes at varying pressurization rates.

Our results indicate that this modulation effect becomes more pronounced when the excitation periods fall within the sensitive range discussed above (Figure 13 and Figure S8 in Supporting Information S1). These sensitive periods approximately match the pre-perturbation recurrence times (t_r^{pre}, Figures 11 and 12, and Figure S7 in Supporting Information S1), suggesting consistency with resonance theory (e.g., Boettcher & Marone, 2004; Guerra et al., 2008; Heuberger et al., 1998). This interpretation differs from that of Beeler and Lockner (2003), who attributed the characteristic failure period to the nucleation time of a stick-slip event. It also contrasts with the model proposed by Savage and Marone (2007), who linked the correlation period to the time scale characterizing state evolution under small perturbations, t^c (Equation 6). As addressed earlier, the correlation period likely corresponds to the characteristic recurrence time of the system (Equation 7).

5.3. Responses to Different Modes of Perturbations and What Governs Acoustic Emissions?

In the present study, different modes of perturbations were explored, including steps, sinusoidal and sawtooth oscillations in normal stress. Due to technical constraints, acoustic measurements were only conducted in two experiments (u828 and u829) that exhibited small-amplitude fluctuations before imposing perturbations. In both experiments, acoustic emission events (AEs) were predominantly observed when rapid changes in σ_n^e occurred, such as during σ_n^e-steps or the sudden imposition of fast sawtooth oscillations (Figure 8). As addressed earlier, exerting sinusoidal oscillations did not generate detectable acoustic events (Figure 14c). We propose that AE generation is intrinsically linked to the slip rate excursions in response to the imposed perturbations, as could be

21699356, 2026, 5, Downloaded from https://agupubs.onlinelibrary.wiley.com/doi/10.1029/2025JB032273 by Tu Delft, Wiley Online Library on [27/05/2026]. See the Terms and Conditions (https://onlinelibrary.wiley.com/terms-and-conditions) on Wiley Online Library for rules of use; OA articles are governed by the applicable Creative Commons License

21699356, 2026, 5, Downloaded from https://agupubs.onlinelibrary.wiley.com/doi/10.1029/2025JB032273 by Tu Delft, Wiley Online Library on [27/05/2026]. See the Terms and Conditions (https://onlinelibrary.wiley.com/terms-and-conditions) on Wiley Online Library for rules of use; OA articles are governed by the applicable Creative Commons License

evaluated from Equation 4, rather than other parameters such as the magnitude or rate of stress drops ($\Delta\tau$ or $|\dot{\tau}|$). Below, we examine this relationship across different experimental stages.

Prior to perturbations, irregular self-sustained shear stress variations occurred without generating any AE (Figure 14c). Despite substantial stress fluctuations ($\Delta\tau > 2$ MPa), the stress drop rates remained relatively low, with de-stressing rates $|\dot{\tau}| < 8.5$ MPa/s, and the excess slip rates (Δv_s) were generally below 42 μm/s (assuming a shear stiffness of 200 MPa/mm, Figure 4).

The shear stress response to an upward step in normal stress generally followed the multi-stage evolution originally described by Linker and Dieterich (1992), except that small-amplitude instabilities emerged immediately after the initial elastic-loading curve (Figure 3). A continuous, single-stage evolution similar to that reported by Prakash (1998) was also observed in our experiments, but only at room temperature, where the gouge exhibits velocity-strengthening and stable sliding behavior (Figure S2 in Supporting Information S1). As discussed by Chen et al. (2024), there is no strict boundary between multi-stage and single-stage response; rather, the observed behavior is governed by the magnitude of slip-velocity excursion induced by the normal stress step, which depends on the frictional velocity dependence of the fault. In general, for any perturbation, a v-weakening fault is expected to experience a much larger excursion in slip-velocity than a v-strengthening one. Following an up-step in normal stress, the slip rate on a v-weakening fault—such as in our hydrothermal experiments—can decrease by several orders of magnitude (Shreedharan et al., 2019). As a result, the fault effectively becomes "stuck", and shear stress tends to follow an elastic-loading curve, consistent with our observations (Figures 3 and 9).

AEs were triggered during all investigated downward normal-stress steps, with the associated $|\dot{\tau}|$ values increasing systematically with step size and generally exceeding 47.9 MPa/s (Figure 9b). AEs were also observed during sudden up-steps. Although the accompanying stress drops were small (<0.5 MPa), they were also rapid, with $|\dot{\tau}|$ reaching up to 24.0 MPa/s and increasing with step size. Importantly, when $|\dot{\tau}|$ is converted into slip velocity using Equation 4, the up- and down-step data collapse onto a single trend (Figure 9e). This reveals a clear linear relation between slip velocity and our proxy for AE event magnitude, showing a lower-bound triggering velocity of ~70 μm/s for the present system (i.e., 70-fold the loading velocity, Figure 9e). This correlation between seismicity and slip rate is broadly consistent with the theoretical expectations from RSF (Segall & Lu, 2015) and filed observations from in situ fluid-injection experiment (Guglielmi et al., 2015), both of which indicate that enhanced slip rate is a key driver for induced seismicity.

When fast sinusoidal ${\sigma_n}^e$-oscillations were applied, the resulting shear stress drop became more rapid. Although $|\dot{\tau}|$ reached up to 23.5 MPa/s—a value comparable to those observed during up-steps—no significant AEs were detected (Figures 8 and 14). However, the absence of AE is consistent with the relatively low slip rates produced during these oscillations (e.g., ~16 μm/s, Figure 14), which remained below the AE-triggering threshold inferred above.

In contrast, abruptly imposing sawtooth-shaped oscillations generated significantly faster stress drops, with $|\dot{\tau}|$ reaching 51.2 MPa/s (Figure 8b). In this case, the corresponding slip rate exceeded 100 μm/s—surpassing the AE-triggering threshold—resulting in clearly detectable events (Figure 8c). All these behaviors at different stages support that the onset of AE activity is controlled principally by slip-rate excursions rather than by the magnitude or rate of the stress change alone.

Finally, we note that the AEs associated with σ_n^e-up-steps suggest failure occurring near a phase of 1.5π — a rarely reported failure phase. We consider it unlikely that this behavior results from technical artifacts in the loading system (e.g., control overshoot), because (a) these events also occurred during relatively small-amplitude steps that were well controlled by the servo system (Figure 9b), and (b) each AE was accompanied by a tiny but rapid stress drop, a response that only arises in the v-weakening regime (see also Chen et al., 2024) and therefore reflects intrinsic frictional (in)stability of the fault. Supporting evidence comes from direct-shear experiments on granite under normal stress perturbations (Huang et al., 2016), which demonstrated that when amplitudes exceed a threshold (~6%), stick-slip failure correlates with oscillatory phases, occurring primarily at 0.5π and 1.5π—the phases corresponding to the maximum destressing and stressing rate, respectively. Consistently, our oscillation tests also revealed "doubling" instabilities at both 0.5π and 1.5π (Figure S8 in Supporting Information S1). Although the mechanism responsible for failure at 1.5π remains unclear, this observation may provide insights

21699356, 2026, 5, Downloaded from https://agupubs.onlinelibrary.wiley.com/doi/10.1029/2025JB032273 by Tu Delft, Wiley Online Library on [27/05/2026]. See the Terms and Conditions (https://onlinelibrary.wiley.com/terms-and-conditions) on Wiley Online Library for rules of use; OA articles are governed by the applicable Creative Commons License

into puzzling field phenomena—such as the seismicity following fluid injection shutdowns (Chang et al., 2018)—where rapid stressing transients may play a role.

5.4. Implications for Natural and Induced Seismicity

5.4.1. Fault Modulation and Enhanced Instability

Our experiments demonstrate that when fault gouge friction initially falls into the unstable regime, frictional instability can be triggered or enhanced by variations in the effective normal stress (σ_n^e) acting on the fault plane. For both *initially fluctuating* and -*stick-slipping* behaviors investigated here, perturbations over a broad range of periods (spanning more than two orders of magnitude) can significantly modulate fault behavior and enhance instability (Figures 11 and 12). Particularly, under *initially stick-slipping* conditions we observed enhanced stress drops with amplitudes that significantly exceed those expected from quasi-steady-state variations (Figure 12). If a natural fault were triggered in this regime, the resulting seismic event could be strongly amplified.

Moreover, the observed failure-prone phases, ranging from 0.5π to 1.0π (Figure 13), indicate that unstable slips are favored by low effective normal stress and fast reductions in σ_n^e. This correlation becomes pronounced under large perturbations, especially when the excitation periods align with those with enhanced events (i.e., 2–100 s). All these results may provide insights into the correlation between regional seismicity and variations in $\sigma_n{}^e$ driven by natural and anthropogenic factors such as solid earth tides, seasonal reservoir discharge, ice sheet melting, and industrial activities into geo-reservoirs (e.g., Beeler & Lockner, 2003).

Our acoustic measurements further revealed that nearly all detected acoustic emission events were associated with rapid $\sigma_n{}^e$-changes, with the proxy of event magnitude being roughly proportional to the magnitude of the $\sigma_n{}^e$-change (Figure 9d). This suggests that larger normal stress or fluid pressure fluctuations increase the seismic triggering potential of a perturbed fault. Recent laboratory injection experiments with varying pressurizing rates demonstrated that cumulative seismic energy scales with the injected fluid volume (e.g., Wang, Kwiatek, Rybacki, Bohnhoff, & Dresen, 2020), a trend reminiscent of our step size dependency and also the volume dependency observed in nature (e.g., Zang et al., 2018).

5.4.2. Reappraisal of Seismic Potentials Under Cyclic Perturbations

Cyclic fluid injection into geo-reservoirs has previously been suggested to cause less induced seismicity than traditional monotonic injections (e.g., Yoon et al., 2014; Zang et al., 2013, 2018). Both in situ and laboratory studies have shown that cyclic injection can reduce not only the number of seismic events but also their maximum magnitude (Zang et al., 2018). However, more recent studies suggest that cyclic injection can promote seismicity at shallow depths (Noël, Passelègue, et al., 2019, Noël, Pimienta, & Violay, 2019). Our experiments—conducted independently of fluid pressure—suggest that cyclic stimulation with short periods may be a relatively safe and efficient strategy. Although such perturbations can induce significant fault slip, the resulting motion is slow and likely to be aseismic (Figure 14).

While this strategy is promising, several caveats must be carefully considered before being applied to geo-reservoir operations. First, these findings do not directly translate to fluid pressure cycling where additional processes—such as diffusion, dilatation, and poroelastic effects—complicate the response (e.g., Cappa et al., 2019; Chambon & Rudnicki, 2001). Second, aseismic slip is not inherently benign: it can redistribute stress to adjacent structures and potentially trigger seismicity elsewhere (e.g., Guglielmi et al., 2015). Third, identifying an optimal cycling period that causes weakening while maintaining stimulation efficiency remains an outstanding challenge. Fourth, given that numerous factors influence the characteristic recurrence time of a fault (i.e., t_r^c, if present, Equation 7), it is crucial to assess the (ir)relevance of t_r^c to the periodicity of fluid injection into or extraction from geo-reservoirs. If the imposed period aligns with the natural recurrence time of the fault, cyclic operations could instead induce fault reactivation. Therefore, field operations—whether cyclic or monotonic—should be designed with consideration of both fluid pressure amplitude and period, as well as the spatial and temporal evolution of these on pre-existing fault planes, as also suggested by previous studies (e.g., Vidal et al., 2019).

Beyond its relevance to human-induced seismicity, our findings on vibration-induced weakening may offer insights into the triggering of avalanches (e.g., Podolskiy et al., 2010), landslides (e.g., Johnson et al., 2017), or aseismic earthquakes (Luo et al., 2025) by (remote) seismic waves. While our experiments do not directly

21699356, 2026, 5, Downloaded from https://agupubs.onlinelibrary.wiley.com/doi/10.1029/2025JB032273 by Tu Delft, Wiley Online Library on [27/05/2026]. See the Terms and Conditions (https://onlinelibrary.wiley.com/terms-and-conditions) on Wiley Online Library for rules of use; OA articles are governed by the applicable Creative Commons License

simulate seismic waves, they represent stress perturbations analogous to those induced by wave-driven strain in faults or rock-sliding interfaces. A well-documented example is aftershock sequences, where triggered events predominantly occur near the mainshock rupture due to static stress changes. However, remote seismic triggering—where seismic waves activate distant faults—suggests an additional dynamic effect. Traditional Coulomb stress analysis (Hill et al., 1993) assumes a critically stressed fault, but our results highlight a strong weakening mechanism triggered by rapid vibrations. This suggests that fault failure can occur even when the fault is not initially critically stressed.

Similarly, this weakening mechanism may influence rupture propagation. Ruptured fault areas radiate seismic waves across a broad frequency spectrum, causing transient fluctuations in fluid pressure and effective normal stress along the fault plane (Bodin et al., 1998; Ferdowsi et al., 2015). We propose that high-frequency normal stress vibrations from seismic waves—originating in slipped regions and arriving at rupture fronts—may help sustain earthquake rupture by dynamically reducing shear strength. This mechanism differs from fluidization effects (Johnson et al., 2008) and could play a crucial role in maintaining and propagating transient slip pulses during seismic events.

6. Conclusions

In this study, we conducted effective normal stress ($\sigma_n{}^e$) perturbation tests on carbonate fault gouges under hydrothermal conditions. We observed two distinct effects by imposing perturbations of specific periods.

First, our results reveal that for faults under deformation in the v-neutral or v-weakening regime, frictional instability can be reinforced under varying normal stress conditions, particularly when the perturbation periods approach or exceed the characteristic recurrence time associated with pre-perturbation instabilities ($t_{\text{imp}} \geq t_r^{\text{pre}}$). Specifically,

1. In the faults that initially showed small-amplitude fluctuations, τ-variations exhibited strong nonlinear responses, including doubling and irregular behaviors under oscillatory normal stress. The associated fault slip was typically limited to a few tens of times the load-point velocity.
2. In the faults that initially showed stick-slip behavior, normal stress oscillations enhanced the stick-slip events, leading to increased stress drop, slip rate, and recurrence time.
3. The most significant unstable slip events occurred preferentially within phases of normal stress oscillation between 0.5π and 1π, corresponding to the maximum rate of stress drop and minimum effective normal stress, respectively.

Second, our results also reveal that short-period perturbations ($t_{\text{imp}} \ll t_r^{\text{pre}}$) can induce fault weakening, which is associated with slow, aseismic deformation. In contrast, abrupt normal stress steps triggered bursts of acoustic emission (AE) events, suggesting a link between AE activity and slip rates.

1. Imposing short-period oscillations was found to reduce shear strength by up to 10%, inducing significant fault slip. These slip events—occurring at velocities less than a few tens of times the loading velocity—were largely aseismic.
2. Short-period oscillations appeared to exert a stabilization effect, suppressing the intrinsic shear stress fluctuations seen before imposing perturbations. Similar effects have been reported in mechanical engineering (e.g., Bureau et al., 2000; Heuberger et al., 1998), where fast normal stress variations are used to control friction.
3. Most AE events in this study were linked to step-changes in normal stress, leading us to propose that seismic events result from slip rate excursions at least 70-fold the loading velocity in the present system.

Taken together, our findings emphasize the importance of excitation periods in fault stability. In the context of induced seismicity, field operations—whether cyclic or monotonic—should be guided by both the amplitude of pressure perturbations and their period. Notably, cyclic injection with periods shorter than some characteristic time scales inherent in the fault system (e.g., $t_{\text{imp}} \leq t^c = D_c/v_{\text{imp}}$) may offer a viable strategy for mitigating seismic risk.

Conflict of Interest

The authors declare no conflicts of interest relevant to this study.

Availability Statement

The data files used in this paper are available at Chen, Niemeijer, and Jansen (2025).

Acknowledgments
This study is co-supported by China National Science Foundation (U2539202, 4217040794, 52227901), and the DeepNL project (Science4Steer: DEEP.NL.2018.046) financed by the Dutch Research Council (NWO).

References

Ader, T. J., Ampuero, J.-P., & Avouac, J.-P. (2012). The role of velocity-neutral creep on the modulation of tectonic tremor activity by periodic loading. *Geophysical Research Letters*, *39*(16), L16310. https://doi.org/10.1029/2012GL052326

Barbot, S. (2024). Transient and steady state friction in non-isobaric conditions. *Geochemistry, Geophysics, Geosystems*, *25*(2), e2023GC011279. https://doi.org/10.1029/2023GC011279

Barbot, S., Guvercin, S. E., Zhang, L., Zhang, H., & Yang, Z. (2025). Thermobaric activation of fault friction. *Geophysical Research Letters*, *52*(6), e2024GL112959. https://doi.org/10.1029/2024gl112959

Bartlow, N. M., Lockner, D. A., & Beeler, N. M. (2012). Laboratory triggering of stick-slip events by oscillatory loading in the presence of pore fluid with implications for physics of tectonic tremor. *Journal of Geophysical Research*, *117*(B11), B11411. https://doi.org/10.1029/2012jb009452

Beeler, N. M., & Lockner, D. A. (2003). Why earthquakes correlate weakly with the solid Earth tides: Effects of periodic stress on the rate and probability of earthquake occurrence. *Journal of Geophysical Research*, *108*(B8), B2391. https://doi.org/10.1029/2001JB001518

Bindschadler, R. A., King, M. A., Alley, R. B., Anandakrishnan, S., & Padman, L. (2003). Tidally controlled stick-slip discharge of a west Antarctic ice stream. *Science*, *301*(5636), 1087–1089. https://doi.org/10.1126/science.1087231

Bodin, P., Brown, S., & Matheson, D. (1998). Laboratory observations of fault-normal vibrations during stick slip. *JGR*, *103*(B12), 29931–29944. https://doi.org/10.1029/98jb02733

Boettcher, M. S., & Marone, C. (2004). Effects of normal stress variation on the strength and stability of creeping faults. *Journal of Geophysical Research*, *109*(B3), B03406. https://doi.org/10.1029/2003jb002824

Bureau, L., Baumberger, T., & Caroli, C. (2000). Shear response of a frictional interface to a normal load modulation. *Physics Reviews E.*, *62*(5), 6810–6820. https://doi.org/10.1103/physreve.62.6810

Candela, T., Brodsky, E. E., Marone, C., & Elsworth, D. (2014). Laboratory evidence for particle mobilization as a mechanism for permeability enhancement via dynamic stressing. *Earth and Planetary Science Letters*, *392*, 279–291. https://doi.org/10.1016/j.epsl.2014.02.025

Capozza, R., Rubinstein, S., Barel, I., Urbakh, M., & Fineberg, J. (2011). Stabilizing stick-slip friction. *Physical Review Letters*, *107*(2), 024301. https://doi.org/10.1103/PhysRevLett.107.024301

Capozza, R., Vanossi, A., Vezzani, A., & Zapperi, S. (2009). Suppression of friction by mechnical vibrations. *Physical Review Letters*, *103*(8), 085502. https://doi.org/10.1103/physrevlett.103.085502

Cappa, F., Scuderi, M. M., Collettini, C., Guglielmi, Y., & Avouac, J.-P. (2019). Stabilization of fault slip by fluid injection in the laboratory and in situ. *Science Advances*, *5*(3), eaau4065. https://doi.org/10.1126/sciadv.aau4065

Chambon, G., & Rudnicki, J. W. (2001). Effects of normal stress variations on frictional stability of a fluid-infiltrated fault. *Journal of Geophisical Research*, *106*(B6), 11353–11372. https://doi.org/10.1029/2001jb900002

Chanard, K., Nicolas, A., Hatano, T., Petrelis, F., Latour, S., Vinciguerra, S., & Schubnel, A. (2019). Sensitivity of acoustic emission triggering to small pore pressure cycling perturbations during brittle creep. *Geophysical Research Letters*, *46*(13), 7414–7423. https://doi.org/10.1029/2019GL082093

Chang, K. W., Yoon, H., & Martinez, M. J. (2018). Seismicity rate surge on faults after shut-in: Poroelastic response to fluid injection. *Bulletin of the Seismological Society of America*, *108*(4), 1889–1904. https://doi.org/10.1785/0120180054

Chelidze, T., & Matcharashvili, T. (2013). Triggering and synchronization of seismicity: Laboratory and field data - A review. In K. Konstantinou (Ed.), *Earthquakes – Triggers, environmental impact and potential hazards*. Nova Science Pub.

Chen, J., Niemeijer, A. R., & Jansen, J. D. (2025). Data accompanying paper entitled "Do normal stress vibrations stabilize or destabilize faults? experimental perspectives" [Dataset]. *Mendeley Data, V1*. https://doi.org/10.17632/3ffh8fz2k3.1

Chen, J., Niemeijer, A. R., & Spiers, C. J. (2024). Rapid normal stress oscillations cause weakening and anelastic dilatation in gouge-bearing faults. *Geophysical Research Letters*, *51*(15), e2024GL109755. https://doi.org/10.1029/2024GL109755

Chen, J., Niemeijer, A. R., & Spiers, C. J. (2025). An extended microphysical friction model for variable normal stress conditions. *Journal of Geophysical Research*, *130*(7), e2025JB032033. https://doi.org/10.1029/2025JB032033

Chen, J., & Spiers, C. J. (2016). Rate and state frictional and healing behavior of carbonate fault gouge explained using microphysical model. *Journal of Geophysical Research: Solid Earth*, *121*(12), 8642–8665. https://doi.org/10.1002/2016jb013470

Chen, J., Verberne, B. A., & Niemeijer, A. R. (2020). Flow-to-friction transition in simulated calcite gouge: Experiments and microphysical modelingssss. *Journal of Geophysical Research: Solid Earth*, *125*(11), e2020JB019970. https://doi.org/10.1029/2020JB019970

Chen, J., Verberne, B. A., & Spiers, C. J. (2015). Interseismic re-strengthening and stabilization of carbonate faults by "non-Dieterich" healing under hydrothermal conditions. *Earth and Planetary Science Letters*, *423*, 1–12. https://doi.org/10.1016/j.epsl.2015.03.044

Cochard, A., Bureau, L., & Baumberger, T. (2003). Stabilization of frictional sliding by normal load modulation. *Journal of Applied Mechanics*, *70*(2), 220–226. https://doi.org/10.1115/1.1546241

Colledge, M., Aubry, J., Chanard, K., Pétrélis, F., Duverger, C., Bollinger, L., & Schubnel, A. (2023). Susceptibility of microseismic triggering to small sinusoidal stress perturbations at the laboratory scale. *Journal of Geophysical Research: Solid Earth*, *128*(4), e2022JB025583. https://doi.org/10.1029/2022jb025583

Dang, W., Konietzky, H., Chang, L., & Frühwirt, T. (2018). Velocity-frequency-amplitude-dependent frictional resistance of planar joints under dynamic normal load (DNL) conditions. *Tunnelling and Underground Space Technology*, *79*, 27–34. https://doi.org/10.1016/j.tust.2018.04.038

Den Hartog, S. A. M., Niemeijer, A. R., & Spiers, C. J. (2013). Friction on subduction megathrust faults: Beyond the Illite-muscovite transition. *Earth and Planetary Science Letters*, *373*, 8–19. https://doi.org/10.1016/j.epsl.2013.04.036

Ellsworth, W. L. (2013). Injection-induced earthquakes. *Science*, *341*(6142), 1225942. https://doi.org/10.1126/science.1225942

Ferdowsi, B., Griffa, M., Guyer, R. A., Johnson, P. A., Marone, C., & Carmeliet, J. (2015). Acoustically induced slip in sheared granular layers: Application to dynamic earthquake triggering. *Geophysical Research Letters*, *42*(22), 9750–9757. https://doi.org/10.1002/2015gl066096

French, M. E., Zhu, W., & Banker, J. (2016). Fault slip controlled by stress path and fluid pressurization rate. *Geophysical Research Letters*, *43*(9), 4330–4339. https://doi.org/10.1002/2016gl068893

Gao, J., Luedtke, W. D., & Landman, U. (1998). Friction control in thin-film lubrication. *Journal of Physical Chemistry B*, *102*(26), 5033–5037. https://doi.org/10.1021/jp982150q

21699356, 2026, 5, Downloaded from https://agupubs.onlinelibrary.wiley.com/doi/10.1029/2025JB032273 by Tu Delft, Wiley Online Library on [27/05/2026]. See the Terms and Conditions (https://onlinelibrary.wiley.com/terms-and-conditions) on Wiley Online Library for rules of use; OA articles are governed by the applicable Creative Commons License

Gao, S. S., Silver, P. G., Linde, A. T., & Sacks, I. S. (2000). Annual modulation of triggered seismicity following the 1992 Landers earthquake in California. *Nature*, *406*(3), 500–504. https://doi.org/10.1038/35020045

Griffa, M., Ferdowsi, B., Guyer, R. A., Daub, E. G., Johnson, P. A., Marone, C., & Carmeliet, J. (2013). Influence of vibration amplitude on dynamic triggering of slip in sheared granular layers. *Physics Reviews E.*, *87*(1), 012205. https://doi.org/10.1103/physreve.87.012205

Guerra, R., Vanossi, A., & Urbakh, M. (2008). Controlling microscopic friction through mechanical oscillations. *Physical Review E - Statistical Physics, Plasmas, Fluids, and Related Interdisciplinary Topics*, *78*(3), 036110. https://doi.org/10.1103/physreve.78.036110

Guglielmi, Y., Cappa, F., Avouac, J. P., Henry, P., & Elsworth, D. (2015). Seismicity triggered by fluid injection–induced aseismic slip. *Science*, *348*(6240), 1224–1226. https://doi.org/10.1126/science.aab0476

Heuberger, M., Drummond, C., & Israelachvili, J. (1998). Coupling of normal and transverse motions during frictional sliding. *The Journal of Physical Chemistry B*, *102*(26), 5038–5041. https://doi.org/10.1021/jp9823143

Hill, D. P., Reasenberg, P. A., Michael, A., Arabaz, W. J., Beroza, G., Brumbaugh, D., et al. (1993). Seismicity remotely triggered by the Mgnitude 7.3 Landers, California, earthquake. *Science*, *260*(5114), 1617–1623. https://doi.org/10.1126/science.260.5114.1617

Hong, T., & Marone, C. (2005). Effects of normal stress perturbations on the frictional properties of simulated faults. *Geochemistry, Geophysics, Geosystems*, *6*(3), Q03012. https://doi.org/10.1029/2004gc000821

Huang, Y. M., Ma, S. L., Miao, A. L., & Yang, M. L. (2016). Effect of normal stress perturbation on fricitonal instability: An experimental study. *Chinese Journal of Geophysics*, *59*(3), 931–940.

Jia, Y., Tang, J., Lu, Y., & Lu, Z. (2021). The effect of fluid pressure on frictional stability transition from velocity strengthening to velocity weakening and critical slip distance evolution in shale reservoirs. *Geomechanics and Geophysics for Geo-Energy and Geo-Resources*, *7*, 1–13. https://doi.org/10.1007/s40948-021-00217-w

Johnson, H. P., Gomberg, J. S., Hautala, S. L., & Salmi, M. S. (2017). Sediment gravity flows triggered by remotely generated earthquake waves. *Journal of Geophysical Research: Solid Earth*, *122*(6), 4584–4600. https://doi.org/10.1002/2016jb013689

Johnson, P. A., Carpenter, B., Knuth, M., Kaproth, B. M., Le Bas, P.-Y., Daub, E. G., & Marone, C. (2012). Nonlinear dynamical triggering of slow slip on simulated earthquake faults with implications to Earth. *Journal of Geophysical Research*, *117*(B4), B04310. https://doi.org/10.1029/2011jb008594

Johnson, P. A., Savage, H., Knuth, M., Gomberg, J., & Marone, C. (2008). Effects of acoustic waves on stick–slip in granular media and implications for earthquakes. *Nature*, *451*(7174), 57–60. https://doi.org/10.1038/nature06440

Kilgore, B., Beeler, N. M., Lozos, J., & Oglesby, D. (2017). Rock friction under variable normal stress. *Journal of Geophysical Research*, *122*(9), 7042–7075. https://doi.org/10.1002/2017JB014049

Kilgore, B., Lozos, J., Beeler, N., & Oglesby, D. (2012). Laboratory observations of fault strength in response to changes in normal stress. *Journal of Applied Mechanics*, *79*(3), 031007. https://doi.org/10.1115/1.4005883

Lastakowski, H., G'eminard, J. C., & Vidal, V. (2015). Granular friction: Triggering large events with small vibrations. *Scientific Reports*, *5*(1), 134doi. https://doi.org/10.1038/srep13455

Leeman, J. R., Saffer, D. M., Scuderi, M. M., & Marone, C. (2016). Laboratory observations of slow earthquakes and the spectrum of tectonic fault slip modes. *Nature Communications*, *7*(1), 11104. https://doi.org/10.1038/ncomms11104

Linker, M. F., & Dieterich, J. H. (1992). Effects of variable normal stress on rock friction: Observations and constitutive equations. *Journal of Geophysical Research*, *97*(B4), 4923–4940. https://doi.org/10.1029/92jb00017

Lockner, D. A., & Beeler, N. M. (1999). Premonitory slip and tidal triggering of earthquakes. *Journal of Geophysical Research*, *104*(B9), 20133–20151. https://doi.org/10.1029/1999jb900205

Lowry, A. R. (2006). Resonant slow fault slip in subduction zones forced by climatic load stress. *Nature*, *442*(17), 802–805. https://doi.org/10.1038/nature05055

Luo, H., Zhou, Y., Zhao, Z., Köküm, M., Wang, T., Yue, H., et al. (2025). A new fault slip mode unveiled in the regional dynamic triggering of the 2023 Turkey Kahramanmaraş earthquake sequence. *AGU Advances*, *6*(1), e2024AV001457. https://doi.org/10.1029/2024av001457

Ma, S., Chen, S., Liu, P., Hu, X., Wang, K., & Huang, Y. (2008). Effect of fault jogs on frictional behavior: An experimental study. *Science in China Series D: Earth Sciences*, *51*, 1436–1445.

Melosh, H. J. (1979). Acoustic fluidization: A new geologic process? *Journal of Geophysical Research*, *84*, B13–B7520. https://doi.org/10.1029/jb084ib13p07513

Niemeijer, A., Marone, C., & Elsworth, D. (2010). Frictional strength and strain weakening in simulated fault gouge: Competition between geometrical weakening and chemical strengthening. *Journal of Geophysical Research*, *115*(B10). https://doi.org/10.1029/2009jb000838

Noël, C., Passelègue, F. X., Giorgetti, C., & Violay, M. (2019). Fault reactivation during fluid pressure oscillations: Transition from stable to unstable slip. *Journal of Geophysical Research: Solid Earth*, *124*(11), 10940–10953. https://doi.org/10.1029/2019jb018517

Noël, C., Pimienta, L., & Violay, M. (2019). Time-dependent deformations of sandstone during pore fluid pressure oscillations: Implications for natural and induced seismicity. *Journal of Geophysical Research*, *124*(1), 801–821. https://doi.org/10.1029/2018JB016546

Olsson, W. A. (1988). The effects of normal stress history on rock friction, key questions in rock mechanics. In P. A. Cundall, R. L. Sterling, & A. M. Starfield (Eds.), *Proceedings of the 29th U.S. Symposium* (pp. 111–117). Univ. of Minnesota, Balkema.

Passelègue, F. X., Brantut, N., & Mitchell, T. M. (2018). Fault reactivation by fluid injection: Controls from stress state and injection rate. *Geophysical Research Letters*, *45*(23), 12837–12846. https://doi.org/10.1029/2018GL080470

Perfettini, H., & Schmittbuhl, J. (2001). Periodic loading on a creeping fault: Implications for tides. *Geophysical Research Letters*, *28*(3), 435–438. https://doi.org/10.1029/2000gl011686

Perfettini, H., Schmittbuhl, J., Rice, J. R., & Cocco, M. (2001). Frictional response induced by time-dependent fluctuations of the normal loading. *Journal of Geophysical Research*, *106*(B7), 13455–13472. https://doi.org/10.1029/2000jb900366

Pignalberi, F., Giorgetti, C., Noël, C., Marone, C., Collettini, C., & Scuderi, M. M. (2024). The effect of normal stress oscillations on fault slip behavior near the stability transition from stable to unstable motion. *Journal of Geophysical Research: Solid Earth*, *129*(2), e2023JB027470. https://doi.org/10.1029/2023jb027470

Podolskiy, E. A., Nishimura, K., Abe, O., & Chernous, P. A. (2010). Earthquake-induced snow avalanches: II. Experimental study. *Journal of Glaciology*, *56*(197), 447–458. https://doi.org/10.3189/002214310792447833

Prakash, V. (1998). Frictional response of sliding interfaces subjected to time varying normal pressures. *Journal of Tribology*, *120*(1), 97–102. https://doi.org/10.1115/1.2834197

Putelat, T., Willis, J. R., & Dawes, J. H. (2012). Wave-modulated orbits in rate-and-state friction. *International Journal of Non-Linear Mechanics*, *47*(2), 258–267. https://doi.org/10.1016/j.ijnonlinmec.2011.05.016

Ranjith, K., & Rice, J. R. (2001). Slip dynamics at an interface between dissimilar materials. *Journal of the Mechanics and Physics of Solids*, *49*(2), 341–361. https://doi.org/10.1016/s0022-5096(00)00029-6

21699356, 2026, 5, Downloaded from https://agupubs.onlinelibrary.wiley.com/doi/10.1029/2025JB032273 by Tu Delft, Wiley Online Library on [27/05/2026]. See the Terms and Conditions (https://onlinelibrary.wiley.com/terms-and-conditions) on Wiley Online Library for rules of use; OA articles are governed by the applicable Creative Commons License

Rice, J. R., & Ruina, A. L. (1983). Stability of steady frictional slipping. *Journal of Applied Mechanics*, *50*(2), 343–349. https://doi.org/10.1115/1.3167042

Rivière, J., Lv, Z., Johnson, P. A., & Marone, C. (2018). Evolution of b-value during the seismic cycle: Insights from laboratory experiments on simulated faults. *Earth and Planetary Science Letters*, *482*, 407–413. https://doi.org/10.1016/j.epsl.2017.11.036

Ruina, A. (1983). Slip instability and state variable laws. *Journal of Geophysical Research*, *88*(B12), 10359–10370. https://doi.org/10.1029/jb088ib12p10359

Savage, H., & Marone, C. (2007). Effects of shear velocity oscillations on stick-slip behavior in laboratory experiments. *Journal of Geophysical Research, Solid Earth*, *112B*(B2). https://doi.org/10.1029/2005JB004238

Scholz, C. H. (2019). *The mechanics of earthquakes and faulting*. Cambridge University Press.

Scuderi, M. M., & Collettini, C. (2016). The role of fluid pressure in induced vs. Triggered seismicity: Insights from rock deformation experiments on carbonates. *Scientific Reports*, *6*(1), 24852. https://doi.org/10.1038/srep24852

Scuderi, M. M., Collettini, C., & Marone, C. (2017). Frictional stability and earthquake triggering during fluid pressure stimulation of an experimental fault. *Earth and Planetary Science Letters*, *477*, 84–96. https://doi.org/10.1016/j.epsl.2017.08.009

Segall, P., & Lu, S. (2015). Injection-induced seismicity: Poroelastic and earthquake nucleation effects. *Journal of Geophysical Research: Solid Earth*, *120*(7), 5082–5103. https://doi.org/10.1002/2015jb012060

Segall, P., & Rice, J. R. (1995). Dilatancy, compaction, and slip instability of a fluid-infiltrated fault. *Journal of Geophysical Research*, *100*(B11), 22155–22171. https://doi.org/10.1029/95jb02403

Shimamoto, T., Handin, J., & Logan, J. M. (1980). Specimen-apparatus interaction during stick-slip in a tri axial compression machine: A decoupled two-degree-of-freedom model. *Tectonophysics*, *67*(3–4), 175–205. https://doi.org/10.1016/0040-1951(80)90234-6

Shreedharan, S., Rivière, J., Bhattacharya, P., & Marone, C. (2019). Frictional state evolution during normal stress perturbations probed with ultrasonic waves. *Journal of Geophysical Research*, *124*(6), 5469–5491. https://doi.org/10.1029/2018jb016885

Tanaka, S., Ohtake, M., & Sato, H. (2012). Spatio-temporal variation of the tidal triggering effect on earthquake occurrence associated with the 1982 South Tonga earthquake of Mw 7.5. *Geophysical Research Letters*, *29*(16), L00G26. https://doi.org/10.1029/2002GL015386

Thompson, P. A., & Grest, G. S. (1991). Granular flow: Friction and the dilatancy transition. *Physical Review Letters*, *67*(13), 1751–1754. https://doi.org/10.1103/physrevlett.67.1751

Trzeciak, M., & Sone, H. (2021). Comparison of acoustic emission activity preceding failure and its frequency content for different rock types. In *Poster presented at American geophysican union fall meeting*.

Verberne, B. A., Chen, J., Niemeijer, A. R., de Bresser, J. H., Pennock, G. M., Drury, M. R., & Spiers, C. J. (2017). Microscale cavitation as a mechanism for nucleating earthquakes at the base of the seismogenic zone. *Nature Communications*, *8*(1), 1645. https://doi.org/10.1038/s41467-017-01843-3

Verberne, B. A., Niemeijer, A. R., De Bresser, J. H., & Spiers, C. J. (2015). Mechanical behavior and microstructure of simulated calcite fault gouge sheared at 20–600°C: Implications for natural faults in limestones. *Journal of Geophysical Research: Solid Earth*, *120*(12), 8169–8196. https://doi.org/10.1002/2015jb012292

Verberne, B. A., Spiers, C. J., Niemeijer, A. R., De Bresser, J. H. P., DeWinter, D. A. M., & Plümper, O. (2013). Frictional properties and microstructure of calcite-rich fault gouges sheared at sub-seismic sliding velocities. *Pure and Applied Geophysics*, *171*(10), 2617–2640. https://doi.org/10.1007/s00024-013-0760-0

Vidal, V., Oliver, C., Lastakowski, H., Varas, G., & Géminard, J.-C. (2019). Friction weakening by mechanical vibrations: A velocity-controlled process. *The European Physical Journal E*, *42*(7), 91. https://doi.org/10.1140/epje/i2019-11855-2

Wang, L., Kwiatek, G., Rybacki, E., Bohnhoff, M., & Dresen, G. (2020). Injection-induced seismic moment release and laboratory fault slip: Implications for fluid-induced seismicity. *Geophysical Research Letters*, *47*(22), e2020GL089576. https://doi.org/10.1029/2020GL089576

Wang, L., Kwiatek, G., Rybacki, E., Bonnelye, A., Bohnhoff, M., & Dresen, G. (2020). Laboratory study on fluid-induced fault slip behavior: The role of fluid pressurization rate. *Geophysical Research Letters*, *47*(6), e2019GL086627. https://doi.org/10.1029/2019gl086627

West, M., Sánchez, J. J., & McNut, S. R. (2005). Periodically triggered seismicity at Mount Wrangell, Alaska, after the Sumatra earthquake. *Science*, *308*(5725), 1144–1146. https://doi.org/10.1126/science.1112462

Wortel, G., Dauchot, O., & van Hecke, M. (2016). Criticality in vibrated frictional flows at a finite strain rate. *Physical Research Letter*, *117*, 198002.

Xing, T., Zhu, W., French, M., & Belzer, B. (2019). Stabilizing effect of high pore fluid pressure on slip behaviors of gouge-bearing faults. *Journal of Geophysical Research: Solid Earth*, *124*(9), 9526–9545. https://doi.org/10.1029/2019jb018002

Yoon, J. S., Zang, A., & Stephansson, O. (2014). Numerical investigation on optimized stimulation of intact and naturally fractured deep geothermal reservoirs using hydro-mechanical coupled discrete particles joints model. *Geothermics*, *52*, 165–184. https://doi.org/10.1016/j.geothermics.2014.01.009

Yu, B., Chen, J., Spiers, C. J., Ma, S., Zhang, M., Qi, W., & Chen, H. (2024). Frictional properties of simulated fault gouges subject to normal stress oscillation and implications for induced seismicity. *Journal of Geophysical Research: Solid Earth*, *129*(9), e2024JB029521. https://doi.org/10.1029/2024jb029521

Zaloj, V., Urbakh, M., & Klafter, J. (1999). Modifying friction by manipulating normal response to lateral motion. *Physical Review Letters*, *82*(24), 4823–4826. https://doi.org/10.1103/physrevlett.82.4823

Zang, A., Yoon, J. S., Stephansson, O., & Heidbach, O. (2013). Fatigue hydraulic fracturing by cyclic reservoir treatment enhances permeability and reduces induced seismicity. *Geophysical Journal International*, *195*(2), 1282–1287. https://doi.org/10.1093/gji/ggt301

Zang, A., Zimmermann, G., Hofmann, H., Stephansson, O., Min, K.-B., & Kim, K. Y. (2018). How to reduce fluid-injection-induced seismicity. *Rock Mechanics and Rock Engineering*, *52*(2), 475–493. https://doi.org/10.1007/s00603-018-1467-4

Zhou, W. (2020). *Investigating the Groningen gas reservoir: From passive seismic monitoring to experiments on effects of pore pressure on fault slip*. Utrecht University.

Zhuang, L., Kim, K. Y., Jung, S. G., Diaz, M. B., Min, K.-B., Park, S., et al. (2016). Laboratory study on cyclic hydraulic fracturing of pocheon granite in Korea. In *50th US rock mechanics/geomechanics symposium* (pp. 16–163). American Rock Mechanics Association. ARMA.

21699356, 2026, 5, Downloaded from https://agupubs.onlinelibrary.wiley.com/doi/10.1029/2025JB032273 by Tu Delft, Wiley Online Library on [27/05/2026]. See the Terms and Conditions (https://onlinelibrary.wiley.com/terms-and-conditions) on Wiley Online Library for rules of use; OA articles are governed by the applicable Creative Commons License